International Journal of Heat and Mass Transfer 239 (2025) 126475

Contents lists available at ScienceDirect

International Journal of Heat and Mass Transfer

journal homepage: www.elsevier.com/locate/hmt

Influence of swirl number and air preheating on turbulent mixing in hydrogen–methane blends within a swirl-stabilized burner

Amin Bekhradinasab [a], Shidvash Vakilipour [a], Jafar Al-Zaili [b,*]

[a] Faculty of New Sciences and Technologies, University of Tehran, Tehran, Iran
[b] Department of Engineering, City, University of London, Northampton Square, London, UK

ARTICLE INFO

Keywords:
Mixing characteristics
Hydrogen blended fuel
Swirl-stabilized burner
Large Eddy simulation
Turbulent flow
OpenFOAM

ABSTRACT

This study investigates the effects of swirl number and air preheating on the turbulent mixing characteristics of pure methane and hydrogen–methane fuel blends in a swirl-stabilized burner. Utilizing large eddy simulations (LES) with the Wall-Adapting Local Eddy-viscosity (WALE) sub-grid model, the turbulent flow fields are calculated and validated using non-reactive cases with varying swirl numbers. The research explores the combined impact of varying swirl numbers, preheating intake air, and hydrogen addition on flow structures and mixing behavior. This integrated approach clarifies how these factors influence flow field structures, stoichiometric volume and length, intensity of segregation, scalar dissipation rate, variance spectral density, and probability density function of mixture fraction. These insights can enhance the efficiency and cleanliness of hydrogen–methane combustion technologies. The findings offer a guidance for optimizing hydrogen–methane fuel blends, contributing to the transition towards sustainable energy sources.

1. Introduction

Despite years of research, understanding the physics of turbulence remains one of the greatest challenges for the scientific community. As a result, questions related to the physics of turbulence continue to pique the interest of scholars and researchers alike. One of the defining characteristics of turbulence is its ability to enhance mixing. The mixing of momentum, energy, and species plays a crucial role in various natural phenomena, from the dissolution of sugar in tea to the formation of solar storms [1]. As a result, the study of turbulent mixing is considered one of the most significant areas of investigation for physicists and engineers.

The depletion of fossil fuel resources, coupled with the resulting price increase, has driven the need for alternative energy sources. Moreover, concerns surrounding climate change and global warming necessitate the use of clean and renewable fuels. As a promising alternative, hydrogen has been proposed due to its high energy density. However, utilizing hydrogen alone poses challenges and requires modifications to existing equipment in various industries. To overcome these challenges, combining hydrogen with hydrocarbon fuels has been identified as a viable solution. Consequently, researchers and engineers are interested in understanding the physics of hydrogen's mixing with other substances, as it holds potential for practical applications.

Mixing patterns can be classified into three distinct levels, with level one referred to as passive scalar mixing [2]. In a turbulent flow field, scalar field fluctuations occur through turbulent convection. These fluctuations, in turn, influence the velocity field through mean gradients and density changes. For small temperature or species concentration differences, the turbulent velocity field drives the scalar field, while the scalar field's impact on the turbulent velocity field is negligible. Thus, this type of mixing does not significantly affect the flow field. In such cases, it is possible to independently determine the passive scalar field by solving the conservation equation of the passive scalar for a given turbulent velocity field [3].

Passive scalar mixing is the simplest form of mixing, yet it has garnered significant attention from researchers due to its wide range of applications and potential for revealing physical phenomena. Numerous studies have focused on scalar spectra, passive scalar fluctuations [4], passive scalar mixing in turbulent jets [5], and passive scalar transport in wall-bounded flows [6]. In a recent study, Bekhradinasab et al. [7] investigated passive scalar transport and mixing in separated flow using Large Eddy Simulation (LES). They discovered that particular attention must be given to the modeled portion of an LES simulation when dealing with passive scalar transport involving Prandtl or Schmidt numbers greater than one. The research also demonstrated a correlation between mixing and Turbulence Kinetic Energy (TKE).

The second level of the mixing paradigm is influenced by various scalars, such as changes in density, viscosity, thermal diffusivity, and

* Corresponding author.
E-mail address: jafar.alzaili@city.ac.uk (J. Al-Zaili).

https://doi.org/10.1016/j.ijheatmasstransfer.2024.126475
Received 21 July 2024; Received in revised form 30 September 2024; Accepted 17 November 2024
Available online 5 December 2024

Nomenclature

ρ	Density of fluid, [kg/m^3]
u	Velocity, [m/s]
p	Pressure, [Pa]
T	Temperature, [K]
λ	Thermal conductivity, [W/(m K)]
C_p	Specific heat capacity, [J/(kg K)]
h_{si}	Sensible enthalpy of spices i, [J/kg]
J_i	Approximate diffusion flux of species i, [kg/m^2 s]
μ_t	Turbulent viscosity, [kg/m s]
Pr_t	Turbulent Prandtl number
Sc_t	Turbulent Schmidt number
M_i	Viscosity or thermal conductivity of species i, [kg/m s or W/(m K)]
D_{ij}	Binary diffusion of species i and j, [m^2/s]
p_{ref}	Standard atmosphere pressure, [Pa]
D_m	Molecular diffusivity, [m^2/s]
D_t	Turbulence diffusivity, [m^2/s]
σ_{ij}	Viscous stress tensor, [kg/m s^2]
τ_{ij}^{sgs}	Turbulent stress tensor, [kg/m s^2]
Y_k	Mass fraction of species k
D_k	Mass diffusivity of species k, [m^2/s]
h_s	Sensible enthalpy, [J/kg]
K	Kinetic energy, [J/kg]
$\overline{\zeta}$	Bilger's mean mixture fraction

mass diffusivity. Direct numerical simulation (DNS) of coaxial jets, conducted by Balarac et al. [8], aimed to investigate the impact of inflow forcing on mixing by generating and controlling vortices. The study evaluated the global mixedness and the intensity of segregation and demonstrated that the forced cases exhibited greater mixing homogeneity than the natural cases at the end of the computational domain. In another experimental study, Alexander Schumaker and Driscoll [9] examined the effect of velocity ratio, density ratio, and Reynolds number on mixing in coaxial jets. For the studied diameter ratios, the stoichiometric mixing lengths were found to be insensitive to the absolute velocity difference between the inner and outer streams and the outer diameter of the outer coaxial jet. The study also identified momentum flux ratio as an effective parameter for predicting stoichiometric mixing length.

The third level of mixing leads to a thorough change in fluid properties, which is particularly evident in combustion. In a study by Masri et al. [10], a new swirl-stabilized burner was introduced as a platform for future experimental and numerical investigations. The burner, namely called the Sydney Swirl Burner (SSB), can stabilize turbulent, non-premixed flames with high swirl numbers and potentially significant turbulence-chemistry correlation. The SSB offers several benefits, including simple and well-defined boundary conditions, along with stabilized swirl, turbulent, and unconfined flames.

Efforts have been made to establish benchmarks for the development of sophisticated numerical tools to compute turbulent, non-premixed flames. Kalt et al. [11] continued these efforts and selected two boundary conditions, named SM1 and SM2, for further investigation, with CNG chosen as the fuel for both. In a study by Al-Abdeli and Masri [12], the effects of changes in boundary conditions on the flow field and blow-off limitation were investigated. The study demonstrated that swirl numbers less than 0.3 did not have any positive effect on blow-off limitation. Furthermore, Malalasekera et al. [13] demonstrated the capability of LES and the laminar flamelet model to predict the structure of turbulent swirling flames. Another study by Vakilipour et al. [14] investigated the effects of CO_2 dilution on the flame structure and temperature distribution in SSB. The study revealed that adding CO_2 reduces both the temperature and length of the flame.

Large-scale coherent structures have a significant influence on combustion and heat release processes by controlling the mixing of fuel and oxidizer [15]. Therefore, a comprehensive understanding of the flow field and coherent structure physics can aid in the development of superior equipment. Swirl flows have received exceptional attention due to their unique properties. When the degree of swirl reaches a certain threshold, the structure of the vortex undergoes a complex transition to a new flow state at some axial regions, known as vortex breakdown, which can lead to the creation of recirculation zones [16]. In certain swirl regimes, flow and mixing patterns are dominated by a three-dimensional time-dependent instability called the precessing vortex core (PVC), which is identified by the center of a vortex precessing around the central axis of symmetry [17]. The vortex breakdown, recirculation zones, and PVC are related swirl flow phenomena that substantially affect mixing and combustion.

Excluding any chemical reactions enables investigation of flow structures without the additional uncertainty related to combustion modeling, which can aid in comprehending the parameters influencing the properties mentioned above and the flow field structure more precisely [18]. The study of non-reactive flows is thus of great importance. In this regard, Al-Abdeli and Masri [19] experimentally investigated non-reactive flow in the SSB to comprehend swirling flows. Their findings revealed that the vortex breakdown resulting in the creation of a recirculation zone depends not only on the swirl number but also on other flow characteristics. Specifically, the study demonstrated the effect of the axial velocity of the primary swirling air or its Reynolds number on the vortex breakdown. Results for five distinct boundary conditions were reported, of which two cases named N29S054 and N16S159 received major attention. These cases represent medium and high swirl numbers, respectively.

Non-reactive flow in the SSB has been the subject of several studies. Al-Abdeli and Masri [20] conducted experiments with a series of new boundary conditions that were not covered in the previous study. In a separate investigation, Malalasekera et al. [21] utilized LES to investigate isothermal flow in the SSB, and demonstrated the capability of LES to predict oscillatory motions such as PVC. Dinesh and Kirkpatrick [22] examined isothermal swirling flow fields with a concentration on flow recirculation, vortices, oscillations, and instabilities. In a subsequent study, Dinesh et al. [23] evaluated the effect of swirl number on turbulence intermittency in the SSB. Additionally, Yang and Kær [24] presented a comprehensive investigation of the formation and mechanisms of flow structures in the N29S054 and N16S159 cases, and demonstrated the superior precision of the shifted inlet by assessing vorticity fields.

Studies have been conducted on the potential use of hydrogen as a supplement to hydrocarbons [25,26]. These studies indicated that the use of hydrogen as a fuel enhancer improves mixture characteristics, facilitates igniting of low-calorific fuels, and increases the level of heat recirculation [27]. Hashemi et al. [28] investigated the influence of turbulence intensity on NO production in burning a hydrogen–hydrocarbon mixture. The study findings showed that raising air turbulence intensity diminishes NO concentration in the flame zone and at the combustor outlet. Kashir et al. [29]examined blended methane and hydrogen on a swirl burner. The results showed that LES could outperform Unsteady Reynolds Averaged Simulation (URAS) predictions in a fine grid. They discovered that an increase in hydrogen concentration had decreased jet penetration length.

While previous studies have investigated hydrogen mixing and swirl effects individually, a thorough examination of the combined influence of hydrogen blending and air preheating on turbulent mixing in swirl-stabilized burners remains sparse. Air preheating has been shown to improve combustion efficiency [30], but its impact on non-reactive turbulent mixing in hydrogen-methane blends is not well understood. To

address this gap, this study utilizes LES with the WALE sub-grid model to analyze coherent structures and mixing dynamics under different operating conditions. The computational setup is validated with non-reactive cases. A detailed analysis is conducted to assess the effects of swirl number, air preheating, and hydrogen content (40% by volume) on the flow field. To the authors' knowledge, there are limited studies focused on non-reactive hydrogen-methane mixing, particularly in relation to swirl number, preheating, and hydrogen addition. The insights gained from this research will contribute to optimizing hydrogen-methane fuel blends, promoting the development of more efficient and environmentally friendly combustion systems.

2. Mathematical modeling

Turbulent mixing in swirled non-reactive flows is distinctively investigated using LES due to its efficacy in capturing time-dependent and anisotropic phenomena critical in swirl flow dynamics, often missed by RANS simulations. LES, particularly with the WALE sub-grid scale model, has shown promise in handling the complexities of such flows, as demonstrated by studies like De Santis et al. [31], who observed accurate reproduction of the swirl-stabilized burner (SSB) flow field on fine grids. This study extends this methodology by examining the turbulent mixing of methane–hydrogen blends in swirled flows, addressing gaps in our understanding of scale interactions and boundary condition impacts on mixing efficiency.

The non-filtered part of any flow variable ϕ is denoted by $\bar{\phi}$. Favre [32] presented a density-weighted filter operation, $\tilde{\phi} = \overline{\rho\phi}/\bar{\rho}$. The filtered non-dimensional compressible Navier–Stokes equations used in the LES are as follow [33].

$$\frac{\partial \bar{\rho}}{\partial t} + \frac{\partial \bar{\rho}\tilde{u}_j}{\partial x_j} = 0 \tag{1}$$

$$\frac{\partial \bar{\rho}\tilde{u}_i}{\partial t} + \frac{\partial \bar{\rho}\tilde{u}_i\tilde{u}_j}{\partial x_j} = -\frac{\partial \bar{p}}{\partial x_i} + \frac{\partial \bar{\sigma}_{ij}}{\partial x_j} - \frac{\partial \tau_{ij}^{sgs}}{\partial x_j}. \tag{2}$$

Filtered equation of state for ideal gas is used as closure for the equation systems.

The differential diffusion effect is taken into account by the following species and energy equations [34].

$$\frac{\partial(\bar{\rho}\tilde{Y}_k)}{\partial t} + \frac{\partial[\bar{\rho}(\tilde{u}_i + \tilde{v}_{ci})\tilde{Y}_k]}{\partial x_i} = \frac{\partial}{\partial x_i}\left((\frac{\mu_t}{Sc_t} + \bar{\rho}\bar{D}_k)\frac{\partial \tilde{Y}_k}{\partial x_i}\right) + S \tag{3}$$

$$\frac{\partial \bar{\rho}(\tilde{h}_s + \tilde{K})}{\partial t} + \frac{\partial \bar{\rho}\tilde{u}_i(\tilde{h}_s + \tilde{K})}{\partial x_i} = \frac{\partial \bar{p}}{\partial t} + \frac{\partial}{\partial x_i}\left((\frac{\mu_t}{Pr_t} + \frac{\bar{\lambda}}{\bar{C}_p})\frac{\partial \tilde{h}_s}{\partial x_i}\right) + \nabla\cdot\left(\bar{\rho}\sum_i^N \tilde{h}_{si}\tilde{J}_i\right). \tag{4}$$

The S therm in Eq. (3) is the representation of the Soret effect. The $\tilde{v}_{ci}$ is used as the correction velocity to ensure mass conservation. The third term on the right side of Eq. (4) presents the heat flux associated with the diffusion of species with different enthalpies. As a common practice, Pr_t and Sc_t were set to 0.85 and 0.7. The following third-order logarithm (N = 4) polynomial fitting equations specify the dependence of species transport properties on temperature and pressure:

$$\ln M_i = \sum_{n=1}^{N} a_{n,i}(\ln T)^{n-1} \tag{5}$$

$$\ln D_{ij} = \left(\sum_{n=1}^{N} b_{n,ij}(\ln T)^{n-1}\right) p/p_{ref} \tag{6}$$

where M_i is the viscosity or thermal conductivity of species i. The binary diffusion of species i and j is defined by D_{ij}. The Wilke formula [35] was used to compute the mixture viscosity. The thermal conductivity and mass diffusivity of mixture was calculated by mixture-averaged model [36].

Table 1
Grid specifications for the computational domain based on Fig. 1 mesh blocking.

Grid	n_{BF}	n_{B1}	n_{B2}	n_{B3}	n_{B4}	n_{CF}	n_{SA}	n_{BB}	n_{FJ}	n_{Tan}
G1	120	70	28	75	45	36	30	80	11	60
G2	120	70	40	150	55	36	30	80	11	60
G3	120	70	40	150	55	36	30	145	11	60
G4	120	70	40	150	55	36	30	80	11	100

3. Numerical solution method

The three-dimensional flow field is modeled using a computational domain based on SSB geometry. The flow simulations are performed using the OpenFOAM compressible solver based on the pimple algorithm. Zhong et al. [34] initially modified the solver to perform reacting LES calculations. The Lewis number equal one assumption is inaccurate due to the molecular Schmidt number of hydrogen [37]. In addition, the low atomic weight of hydrogen makes it imprecise to neglect the Soret effect. The modification has been carried out to consider binary diffusion and the Soret effect.

The governing partial differential equations are discretized using the cell-centered finite volume method. Temporal terms for momentum and other transport equations are discretized using second-order and first-order implicit schemes, respectively. For convection terms, a limited central differencing scheme is employed, while pure central differencing is used for the Laplacian and gradient schemes. The number of outer loops is dynamically set using the residual control method to maintain the stability of the solution and avoid numerical oscillation caused by second-order discretization. The average number of outer loops varies between four and eight. The maximum Courant number is set 0.6 to 0.9 to ensure the stability of numerical

Boundary conditions for the study are as follows: Dirichlet boundary conditions for inlet velocity, temperature, species, and outlet pressure, while Neumann boundary conditions are applied to outlet velocity, temperature, species, and inlet pressure. A slip boundary condition is used for the lateral boundary. To generate a valid turbulent inlet for the LES, a fluctuating velocity field is created using the Lund transformation. The inlet mass flow rates and temperatures match the SM1 experimental conditions, with hydrogen concentrations of 0% and 40% by volume added to methane for various cases. In hydrogen-enriched cases, the fuel stream contains a blend of hydrogen and methane. Three swirl numbers (0.3, 0.5, and 0.7) are used to explore the effects of hydrogen addition and swirl on mixing mechanisms. Additionally, preheated cases were investigated by increasing the temperature of the swirl and co-flow air by 307 K. In this study, air is considered to consist of 77% mass fraction nitrogen and 23% oxygen. Three cases with a blend of methane and hydrogen as fuel were examined without swirl: one case without preheating, one case with preheating of the fuel, and another with preheating of the air. This setup facilitates a deeper investigation into the effects of swirl on both non-preheated and preheated flow regimes. The boundary conditions used for the different cases are summarized in Table 2.

The computational domain is divided into cylindrical blocks to control the mesh resolution, as illustrated in Fig. 1. The domain itself is developed within a cylinder with a length of 350 mm and a diameter of 158 mm. To ensure fully developed flow conditions at the pipes outlet, the inlet sections are extended 100 mm upstream, as suggested by Yang and Kær [24].

To evaluate the impact of grid resolution and select a proper grid for current computational experiments, four grids are employed, designated as G1, G2, G3, and G4 including 1.8, 2.7, 3.7, and 4.7 million cells, respectively. Table 1 denotes the details of the grid spacing for mesh blocks. The number of grid spacing along the jet flow (x-direction) for mesh blocks block-1 to block-4 are represented by n_{B1} to n_{B4}, respectively. In block-1, the number of grid spacing of the fuel

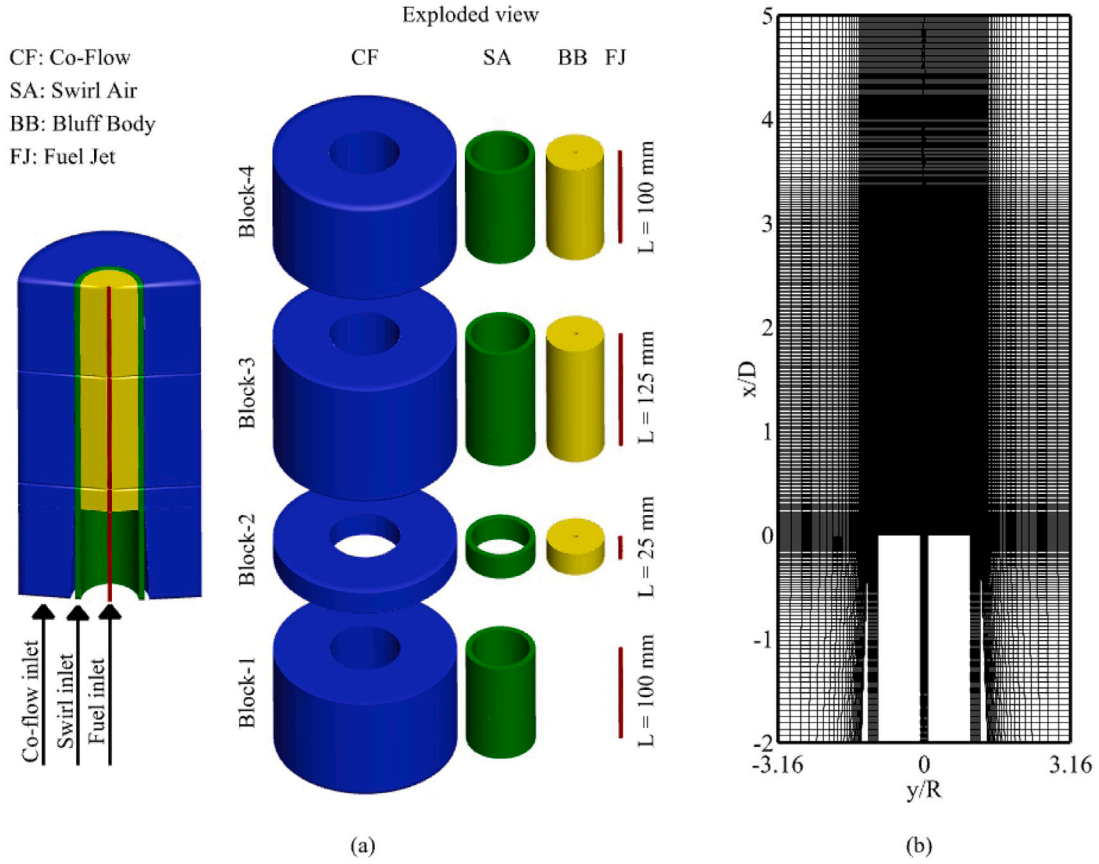

Fig. 1. Description of computational domain: (a) associated cylindrical blocks utilized for controlling mesh resolution, (b) two-dimensional view of grid G2. The plane $z = 0$ represents two-dimensional view where y direction is indicator of radial direction.

Table 2
Boundary condition specifications for co-flow, swirled flow, and fuel line.

Cases	Fuel composition	Swirl and coaxial composition	Fuel temperature (K)	Swirl and coaxial temperature (K)	Swirl number
N29S054	Air	Air	293	293	0.54
N16S159	Air	Air	293	293	1.59
Primary	Methane	Air	293	293	0.5
Primary-H2(40%)	Methane–Hydrogen (blended)	Air	293	293	0.5
Low Swirl	Methane	Air	293	293	0.3
Low Swirl-H2(40%)	Methane–Hydrogen (blended)	Air	293	293	0.3
High Swirl	Methane	Air	293	293	0.7
High Swirl-H2(40%)	Methane–Hydrogen (blended)	Air	293	293	0.7
Preheated	Methane	Air	293	600	0.5
Preheated-H2(40%)	Methane–Hydrogen (blended)	Air	293	600	0.5
No Swirl, No Preheat (NSNP)	Methane–Hydrogen (blended)	Air	293	293	–
No Swirl, Fuel Preheated (NSFP)	Methane–Hydrogen (blended)	Air	600	293	–
No Swirl, Air Preheated (NSAP)	Methane–Hydrogen (blended)	Air	293	600	–

pipe, i.e. n_{BF}, is different from the co-flow and swirl air ducts in the x-direction. The radial direction for each series is represented by n_{CF}, n_{SA}, n_{BB}, and n_{FJ}, while n_{Tan} specifies the number of cells in the tangential direction. A structured mesh generated for the square section in center of the fuel pipe. The number of cells in this section is equal to the square of the number of cells in the tangential direction. The grid was initially generated using cylindrical coordinates, but the numerical calculations are carried out using Cartesian coordinates, which is the framework of OpenFOAM. To ensure consistency between the two coordinate systems, the $z = 0$ plane is selected as the origin plane. In this plane, x, y, and normal directions in Cartesian coordinates correspond to the streamwise, radial, and tangential directions in cylindrical coordinates,

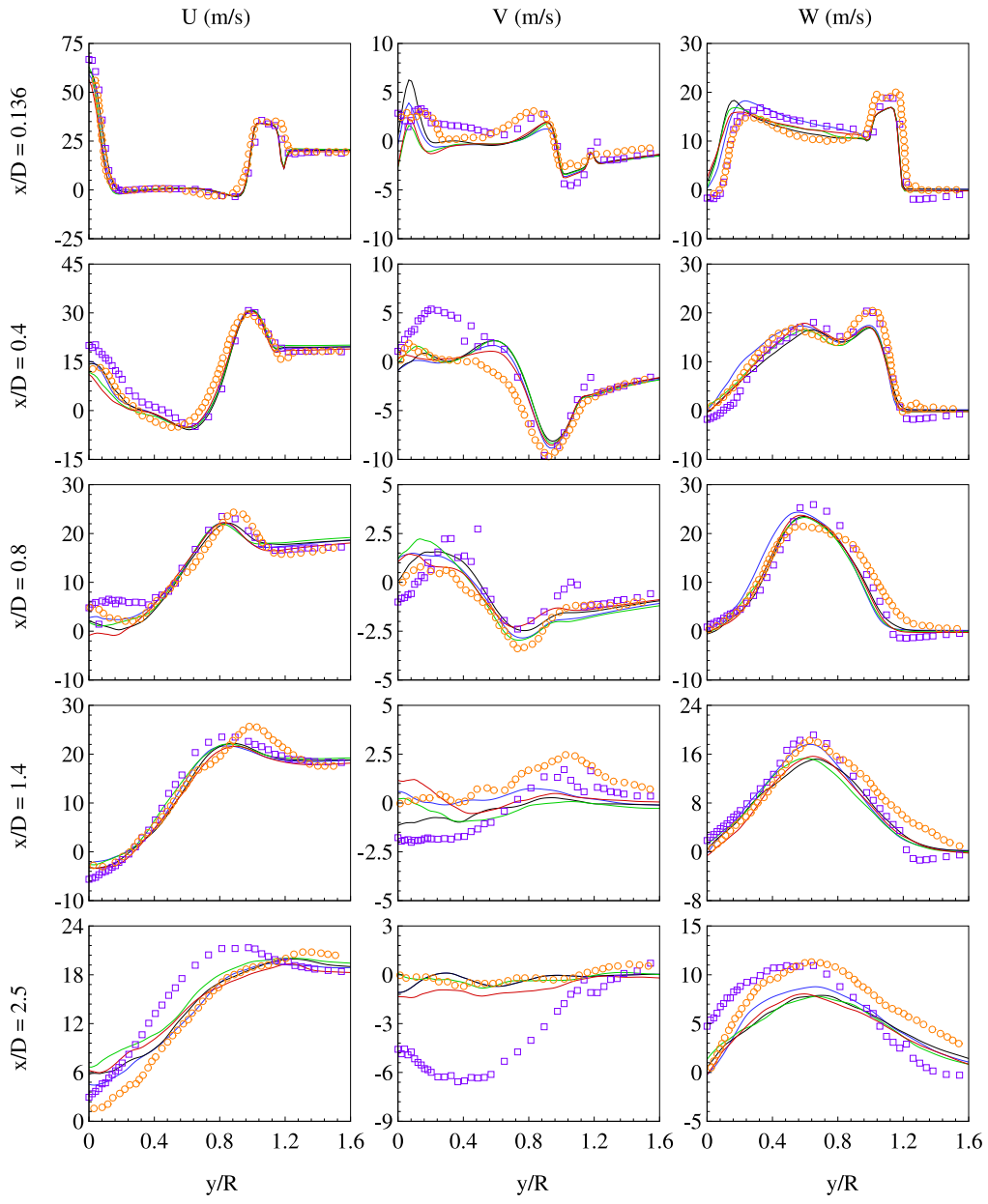

Fig. 2. Comparison of axial, radial, and swirl velocity profiles' of N29S054 with experimental data of Al-Abdeli and Masri [19] (squares) and LES simulation results of Malalasekera et al. [21] (circles). Blue, black, green and red lines indicates G1, G2, G3 and G4 grid results, respectively. (For interpretation of the references to color in this figure legend, the reader is referred to the web version of this article.)

respectively. The reported velocities in this paper also follow this convention. Accordingly, u, v, and w denote the streamwise, radial, and tangential velocities, respectively.

All simulations were run on the Hyperion high-performance computing cluster at City, University of London. Parallel processing was implemented using the OpenMPI distributed memory model, with each case running on four nodes. Each node was equipped with two Intel Xeon Gold 6248R processors and 384 GB of RAM. To ensure reproducibility across cases, the same computational setup (including the number of processors and communication protocols) for all simulations is used.

4. Results and discussion

In this section, the computational grid and numerical settings are validated and verified by simulating two non-reactive cases with medium and high swirls, namely N29S054 and N16S159. The N29S054 case features a bulk axial velocity of 29.74 m/s in the swirl annulus, with a swirl number of 0.54. In contrast, the N16S159 case exhibits a bulk axial velocity of 16.26 m/s in the swirl annulus, accompanied by a higher swirl number of 1.59. The simulation results are utilized to select a proper computational grid. The effects of increasing and decreasing the swirl number, pre-heating the swirl and co-flow air, and adding hydrogen to the fuel are studied and reported in detail to investigate the coherent structure of the flow field and its mixing. The reliability of simulation results is also assessed. These discussions are presented through four subsections: validation and verification, flow fields and coherent structures, mixing characteristics, and turbulence and statistics of mixing.

4.1. Validation and verification

Fig. 2 displays the velocity profiles of N29S054 as compared to experimental data [19] and previous LES results [21] for four different

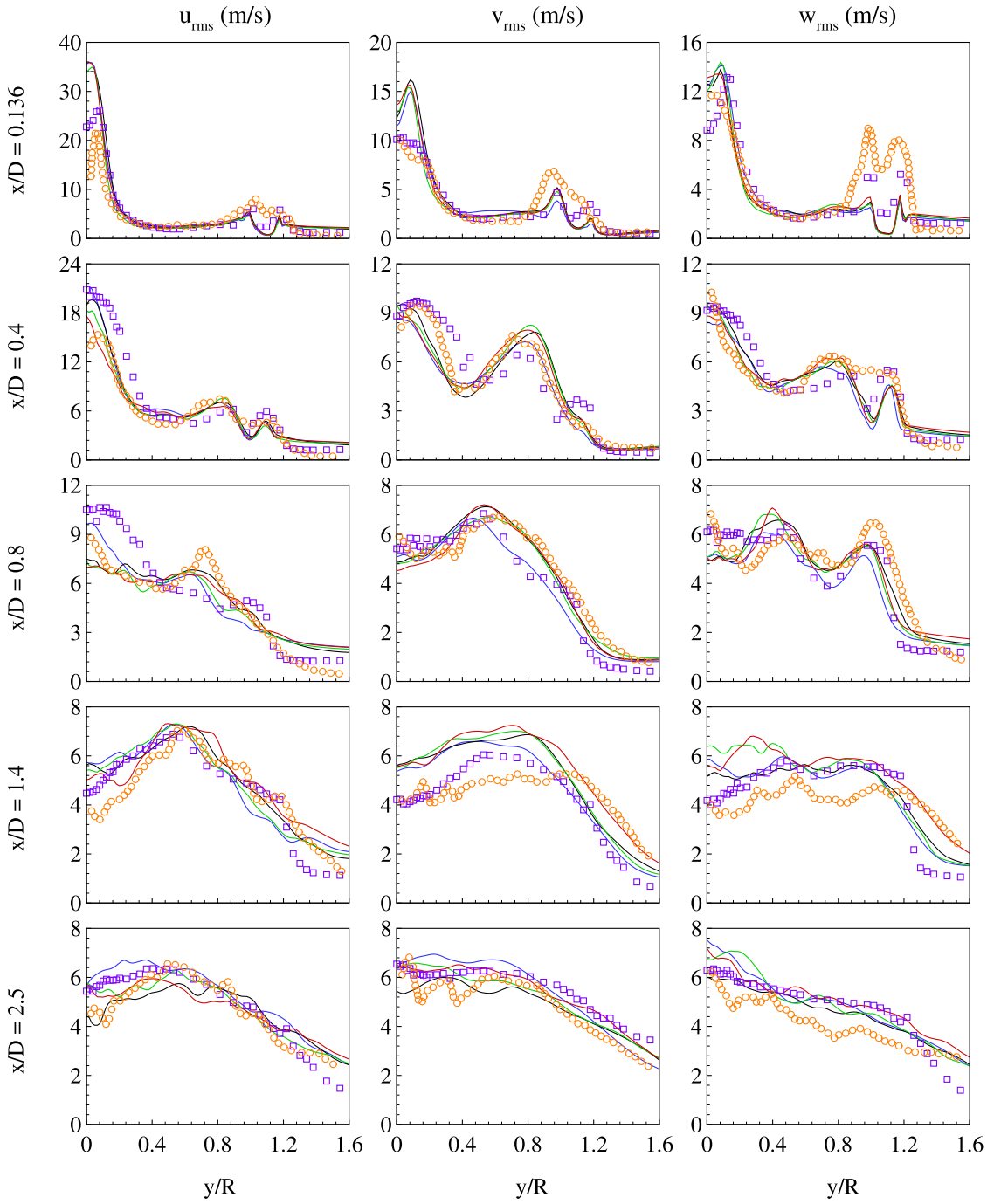

Fig. 3. Comparison of RMS of axial, radial, and swirl velocity profiles of N29S054 with experimental data provided by Al-Abdeli and Masri [19] (squares) and LES results of Malalasekera et al. [21] (circles). Blue, black, green and red lines indicates numerical results obtained on G1, G2, G3, and G4 grids, respectively. (For interpretation of the references to color in this figure legend, the reader is referred to the web version of this article.)

grids: G1, G2, G3, and G4. The presence of a bluff body leads to a reverse flow at x/D = 0.136 and 0.4, which is consistent with experimental data. At x/D = 0.8, the axial velocity profile shows a vortex breakdown that leads to the formation of a recirculation bubble playing a crucial role in combustion and mixing. Nonetheless, a discrepancy is observed between the measurements and LES results for the radial velocity at x/D = 2.5. This is a result of measurement errors affecting the fulfillment of the continuity equation by the radial velocity in the experimental data [24].

Fig. 3 depicts the root mean square (RMS) of velocity fluctuations. The RMS profiles indicates a slight over-prediction of the axial and radial velocity RMS at x/D = 0.136. This makes a dissipation of jet potential core and under-prediction of axial velocity at x/D = 0.136.

The velocity profiles of the N16S159 simulation are shown in Fig. 4. Here, a reverse flow zone is observed between x/D = 0.136 and x/D = 1.4. Unlike the case with medium swirl number, in the case with high swirl number, the reverse flow zones are connected resulting in a large continuous recirculation bubble.

Fig. 5 compares the turbulence intensity of the LES calculations resolved fluctuations and experimental measurements. The RMS of velocity shows an over-prediction of turbulence intensity at x/D = 0.136 in the LES results. Numerical over-prediction results in a faster decay of the fuel jet leading to a lower axial velocity in downstream. This

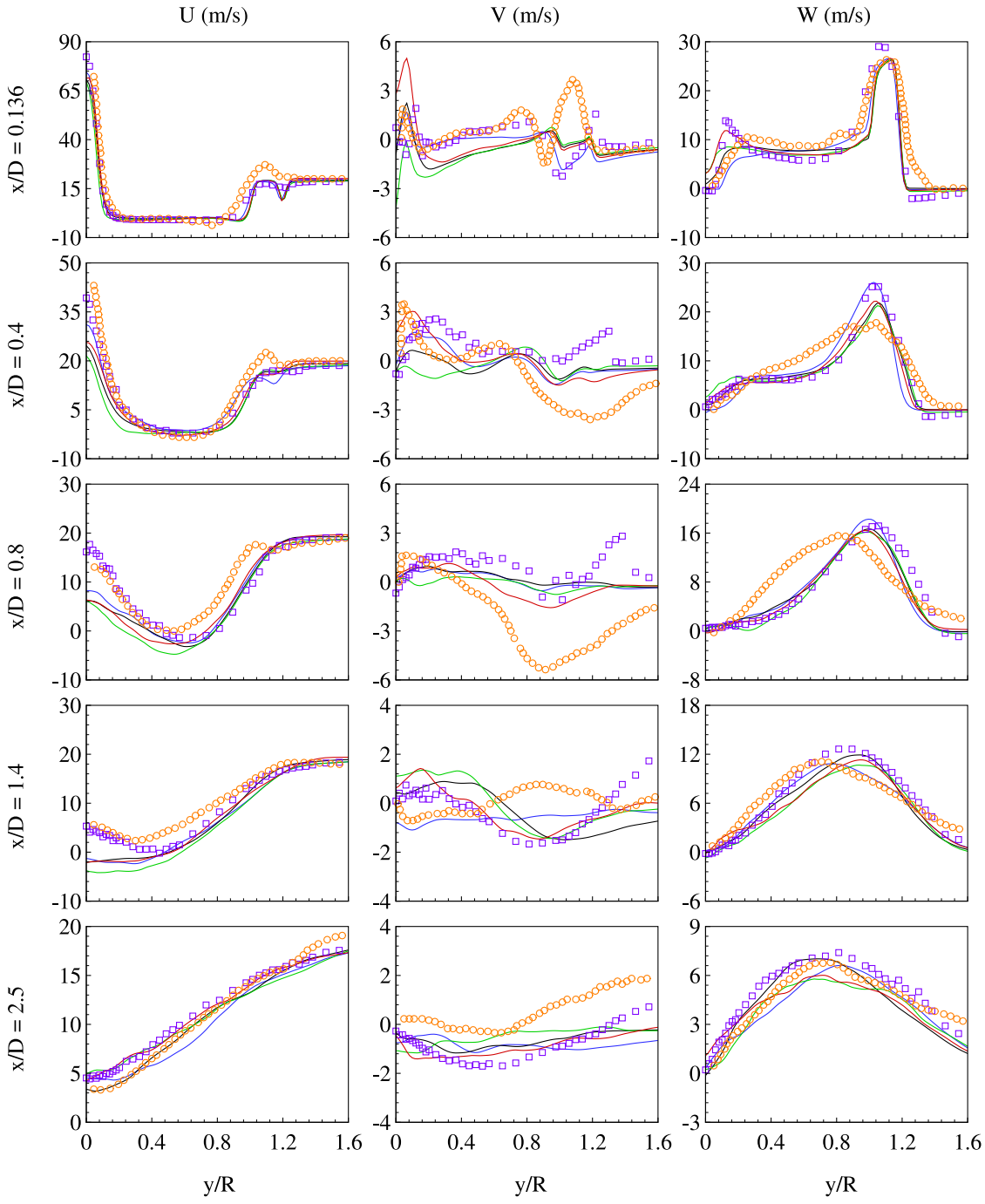

Fig. 4. Comparison of axial, radial, and swirl velocity profiles of N16S159 with experimental data of Al-Abdeli and Masri [19] (squares) and LES simulation results of Malalasekera et al. [21] (circles). Blue, black, green and red lines indicates numerical results obtained on G1, G2, G3 and G4 grids, respectively. (For interpretation of the references to color in this figure legend, the reader is referred to the web version of this article.)

is encountered as a reason for smaller RMS in downstream and larger predicted recirculation zone in comparison to the experimental data.

All computational grids used in this study demonstrated good agreement with experimental data. The mass flow rate and Reynolds number for methane fuel simulations were consistent with the SM1 configuration, while the fuel jet Reynolds number was smaller compared to N29S054 and N16S159 configurations. The co-flow air Reynolds number matched validation cases, while the swirl air Reynolds number was slightly higher. Results show that G1 provided sufficient resolution for LES flow computations, as its velocity profiles matched experimental measurements. However, G2 was preferred for its finer axial mesh, which is more suitable for higher Reynolds numbers in the swirl airflow. Additionally, G2 resolved a higher percentage of turbulent kinetic energy across the domain, providing more accurate flow details compared to G1. Furthermore, adding 40% hydrogen to methane does not significantly change the fuel jet Reynolds number, making G2 well-suited for studying methane–hydrogen blends. Finally, G2 was computationally more efficient than G3 and G4, while still maintaining

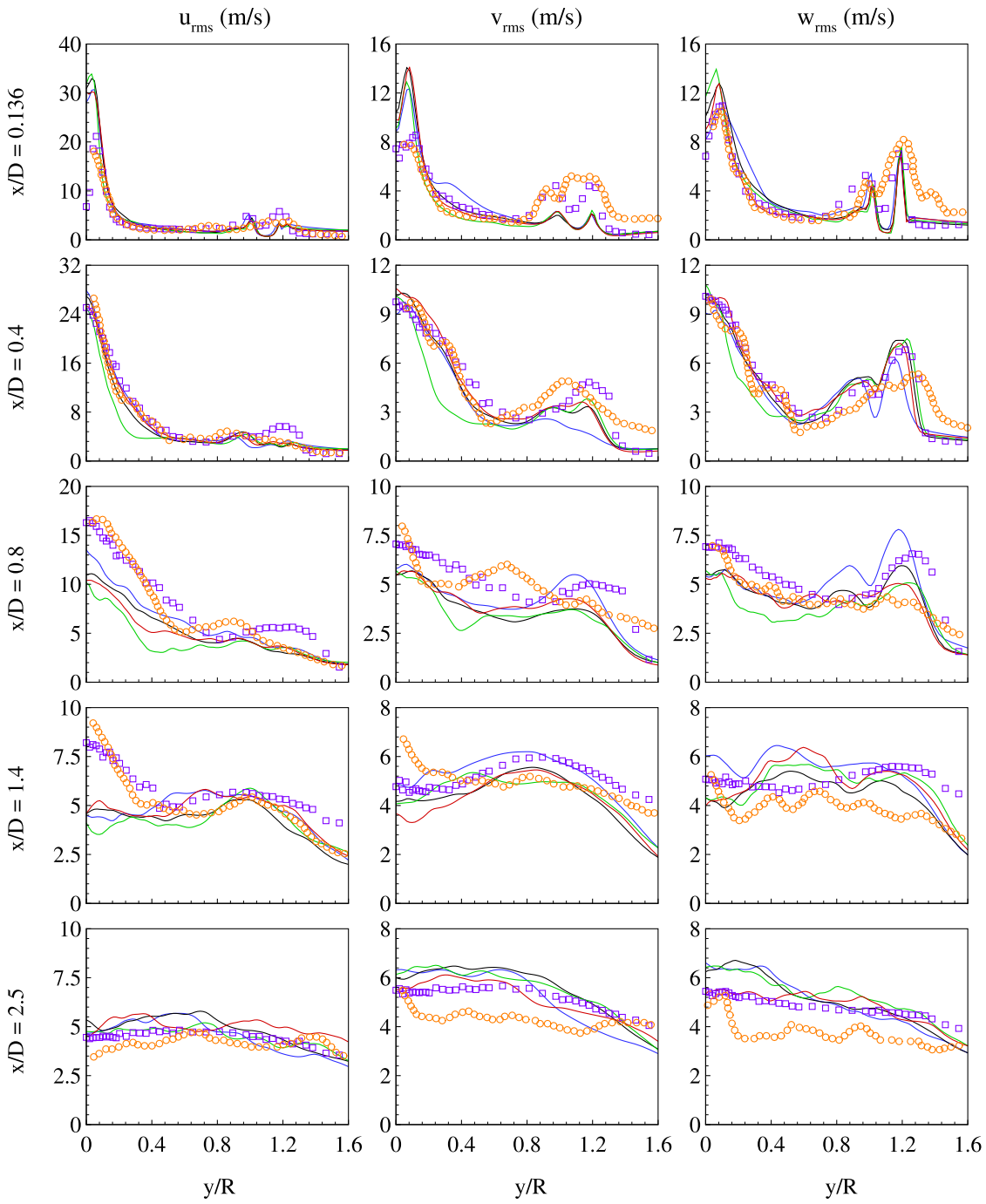

Fig. 5. Comparison of RMS of axial, radial, and swirl velocity profiles' of N16S159 with experimental data of Al-Abdeli and Masri [19] (squares) and LES simulation results of Malalasekera et al. [21] (circles). Blue, black, green and red lines indicates G1, G2, G3 and G4 grid results, respectively. (For interpretation of the references to color in this figure legend, the reader is referred to the web version of this article.)

sufficient resolution for the test cases, making it the optimal choice for this study.

4.2. Flow fields and coherent structures

Fig. 6 shows the axial velocity profiles for the studied mixing flow cases with pure methane and a blend of 40% volumetric (Vol) hydrogen and 60% Vol methane. Preheating the intake air results in a decrease in the air density, leading to an increase in air intake velocity under the assumption of constant mass flow rate. The lowest fuel velocity is predicted at the entrance of the domain for the low swirl flow case. The fuel stream accelerates along the centerline and the highest axial velocity is achieved in downstream of the center of fuel flow. On the other hand, the highest axial velocity is calculated at the fuel pipe exit for the high swirl flow case decreasing toward downstream. The addition of 40% Vol hydrogen to the fuel resulted in an increase in axial velocity of the inlet fuel jet by 60%, 178%, 54%, and 39% in the primary, low swirl, high swirl, and preheated cases, respectively.

Fig. 6 displays the axial variation of the RMS of axial velocity. In this figure, an increase in the turbulence intensity is demonstrated under preheat conditions with a substantial difference compared to other flow cases. The higher RMS value observed at the air inlet is attributed to the increased velocity of air. In the center of the computational domain, it is due to the increased flux momentum ratio. Hydrogen density is

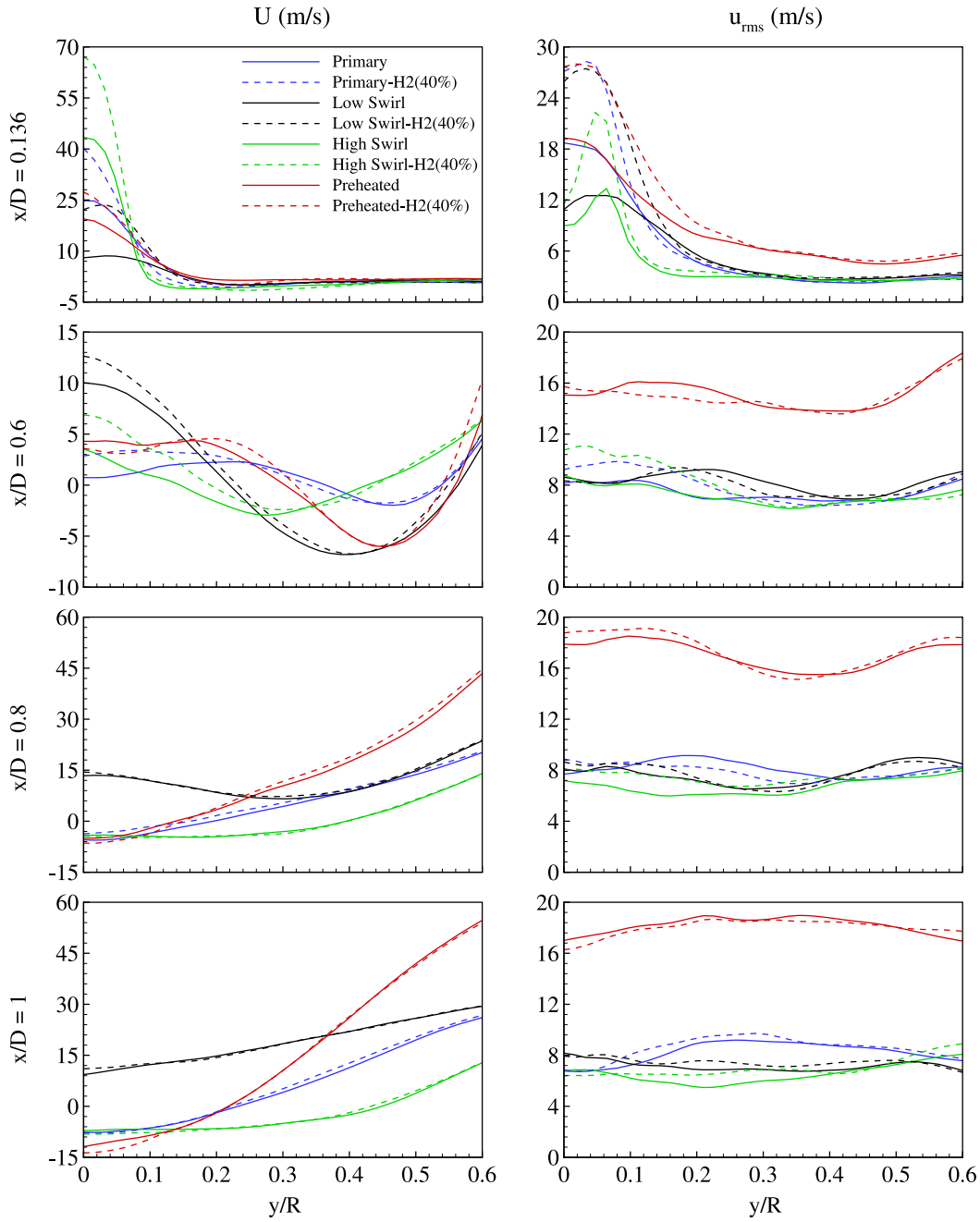

Fig. 6. The axial velocity (left) and the RMS of axial velocity (right) profiles at axial distances of x/D = 0.136, 0.6, 0.8, and 1 for four different cases: primary, low swirl, high swirl, and preheated air. The profiles are presented for methane fuel with solid line and a blend of 40% Vol hydrogen and 60% Vol methane with the dashed line.

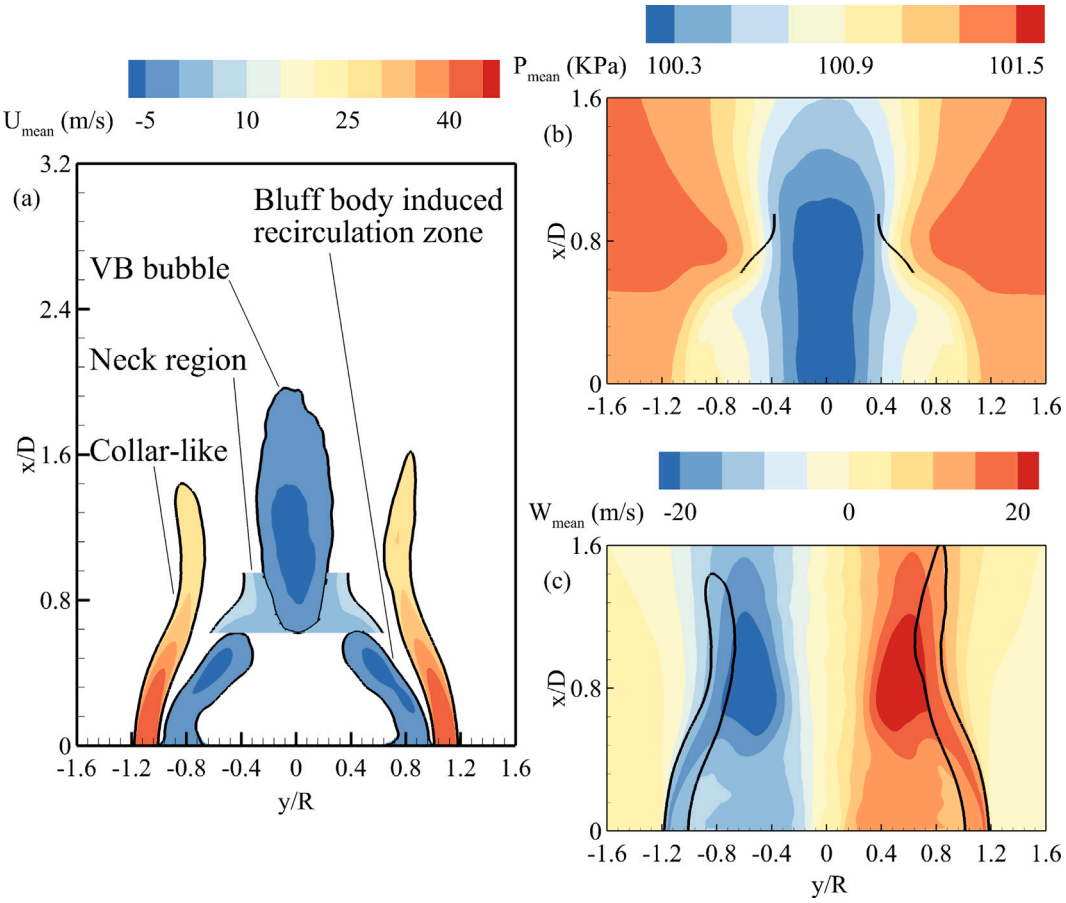

Fig. 7. Flow structures for primary case with methane fuel. (a) axial velocity contour and flow structures. (b) contour of pressure near the neck region. (c) swirl velocity contour around collar-like flow structure.

lower than that of methane and consequently, hydrogen is injected with lower momentum makes it spread more rapidly. Moreover, the Soret effect could further intensify hydrogen spreading. Consequently, more dissipative flow is observed around the fuel inlet, resulting in higher fluctuations in this region.

Fig. 7 demonstrates several flow structures, including recirculation bubble, recirculation zone near the bluff body, neck region and collar-like flow pattern. These flow structures are similar to those observed in the reacting flows, indicating that the complex flow patterns are not significantly altered by the absence of chemical reactions [13,18,38]. Two types of recirculation zones can be identified: toroidal and bubble-shaped recirculation zones. The toroidal recirculation zone stagnates above an obstruction, such as a bluff body, placed in axial flows. Other recirculation zones, formed further downstream, are attributed to the vortex breakdown. The formation of a stagnation point or a region of reversed flow is essential to generate these types of recirculation zones in swirling flows.

The vortex breakdown phenomenon occurs at sufficiently high levels of swirl, characterized by a flow reversal along the centerline. This is caused by a negative pressure gradient resulting from the turbulence effects within the flow. The force imbalance between fluid outward expulsions and axial momentum is responsible for the vortex breakdown [21]. For an axial pressure gradient higher than a critical threshold, the flow reverses and generates a recirculation bubble. In this situation, there is a neck region between the recirculation bubble and bluff body where the pressure drop radially. Due to the significant pressure drop in this region, the swirling velocity is greater than the bulk velocity at the swirl air inlet. Then, a collar-like flow is generated by positive swirl velocities on one side and negative swirl velocities on the other side [13].

Fig. 8 illustrates the contours of the mean axial velocity for all cases, providing valuable insights into the flow patterns that impact the mixing process. In the primary case, the four mentioned above flow structures are observed. As the fuel is blended with hydrogen, the recirculation bubble formed a little downstream but the flow structures remained unchanged. In the low swirl case, there is no vortex breakdown downstream and the recirculation bubble is replaced with a low-velocity region formed downstream of the fuel jet. As the swirl number increased, the central recirculating area expanded and the reversed flow region on the edge of the bluff body extended to the center. The extended reversed flow region is connected to the central recirculation bubble and this enlarged recirculation area confines the fuel–air mixing region. Although, blending fuel with hydrogen does not change the length the recirculation bubble however, it slightly increased its width. Preheating the intake air generates all the flow structures observed in the primary flow case. However, the flow with preheating is driven with a relatively higher axial distribution of velocity in comparison with the primary flow case. These findings suggest that the creation of these flow structures depends solely on the swirl number and mass flow rate of the air and fuel.

Fig. 9 illustrates contours of TKE calculated for the four studied flow cases. As is seen, it is obvious that the highest TKE value in the fuel jet inlet occurs in the pre-heated case, while the lowest TKE value is observed in the high swirl case. The high swirl case exhibits a bubble-like region that generates a low-TKE zone around the fuel jet inlet. In contrast, the preheated case exhibits a higher momentum flux ratio that results in a larger energy difference between layers and higher turbulence intensity, leading to increased TKE. The addition of hydrogen to the fuel increases TKE in all cases. Increase in TKE can be a result of two factors: an increase in the velocity of the fuel

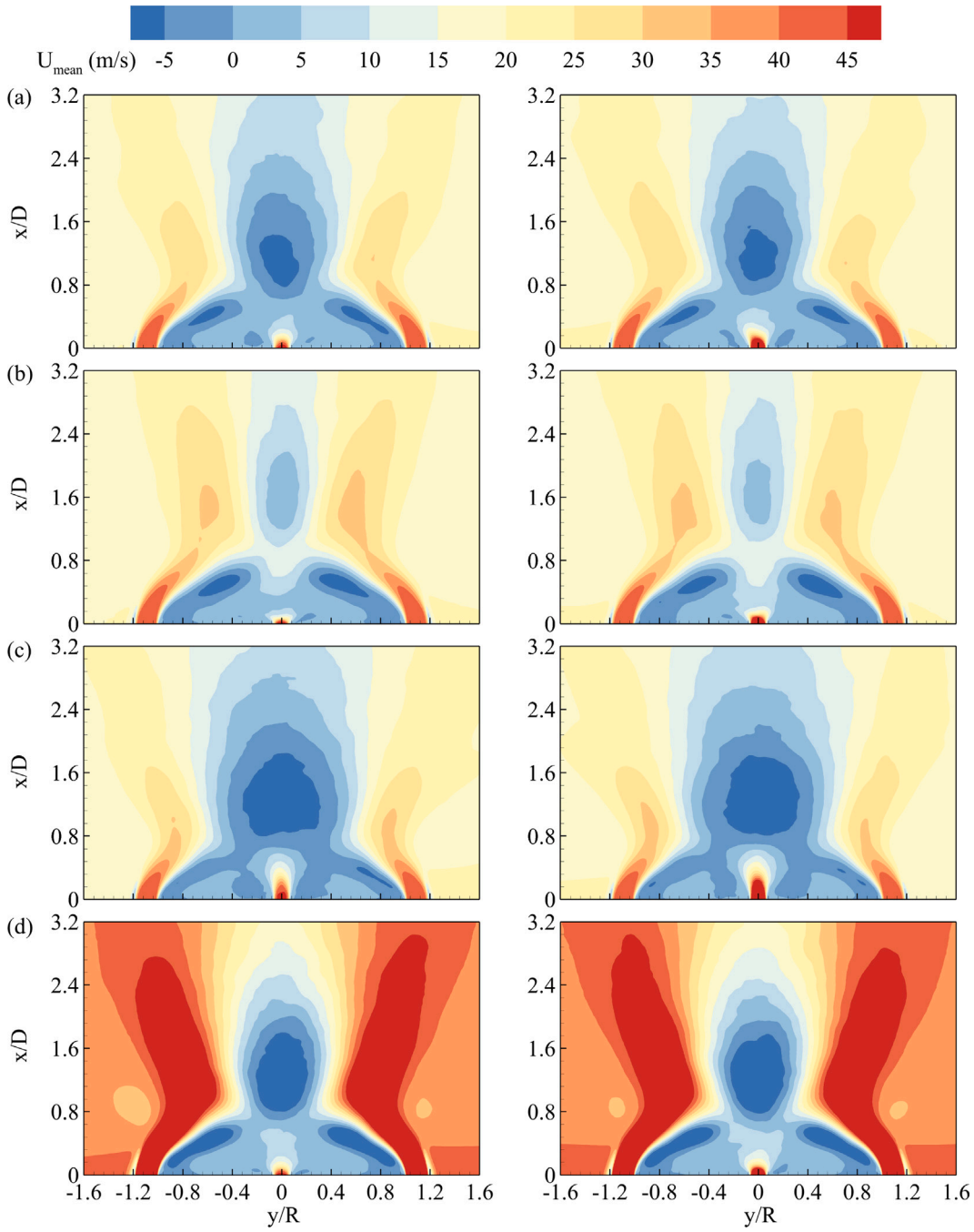

Fig. 8. Axial velocity contours for four different cases: (a) primary, (b) low swirl, (c) high swirl, and (d) preheated air. The contours are presented for both methane fuel (left) and a blend of 40% Vol hydrogen and 60% Vol methane (right).

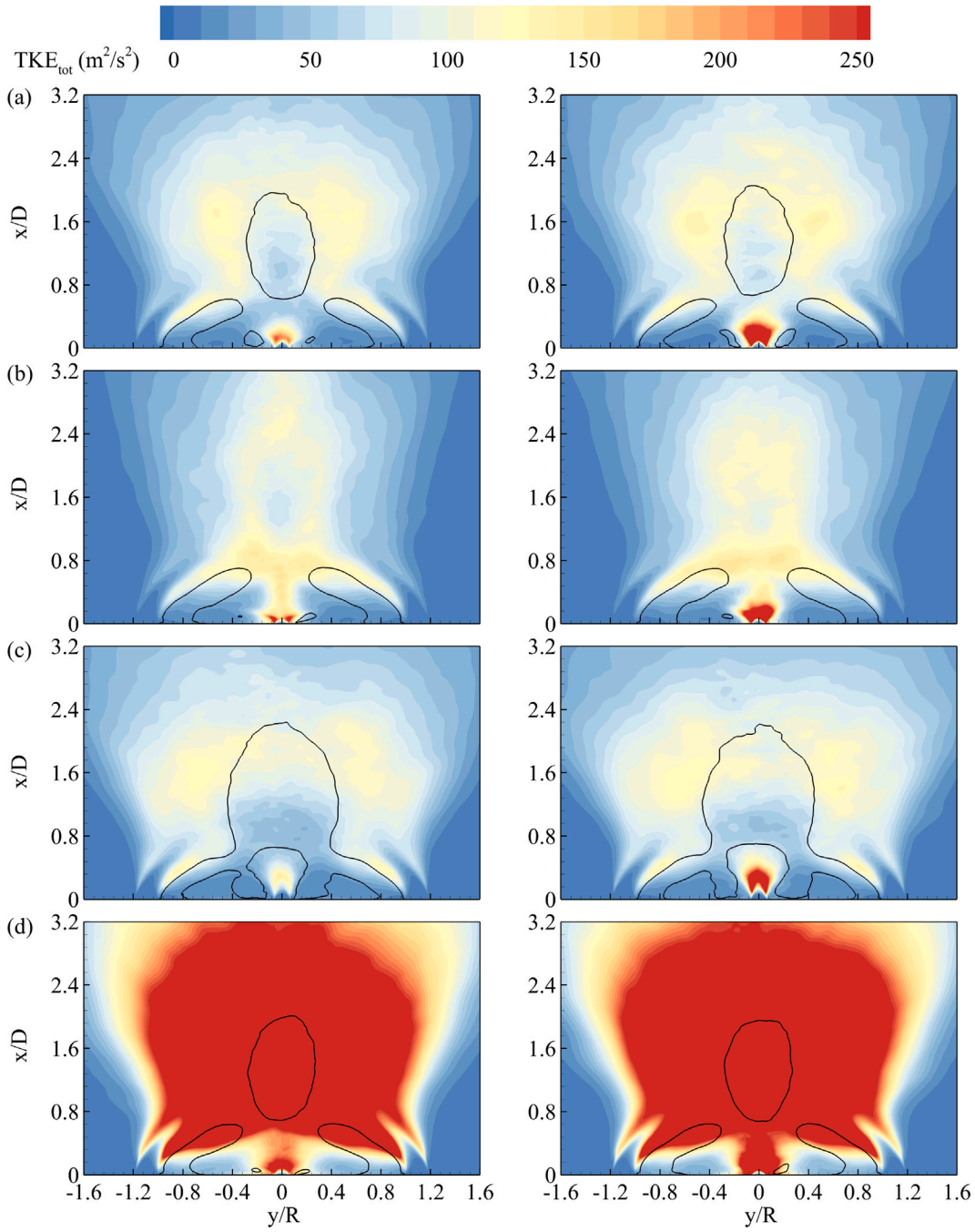

Fig. 9. The TKE contours for four flow cases of (a) primary, (b) low swirl, (c) high swirl, and (d) preheated air. The contours are presented for pure methane fuel (left) and a blended fuel with 40% Vol hydrogen and 60% Vol methane (right). Solid lines indicate the boundary of recirculation zones.

jet due to constant mass flow rate and energy imbalance in the flow structures surrounding the fuel jet stream. This imbalance occurs due to the lower density of hydrogen than methane, resulting in the formation of heterogeneous layers of these two gases. Specifically, hydrogen has a shorter dynamic residence time and experiences faster velocity changes in the flow field due to its lower density. Consequently, the layers of hydrogen and methane exhibit different momentum levels due to differences in velocity and density, giving rise to a local momentum flux that contributes to the increase of TKE. In overall, the present findings suggest that the addition of hydrogen alters the momentum balance and modifies the turbulence intensity, leading to changes in TKE.

4.3. Mixing characteristics

Fig. 10 presents the mixture fraction profiles at different axial positions. In this study, Bilger's definition of mixture fraction is used to discuss the numerical results of the mixing flow simulations [39]. The high swirl case exhibits concentration of mixture fraction at the center, specifically at sections x/D = 0.136, 0.6, and 0.8. This concentration is attributed to the presence of a low TKE bubble-like region near the fuel inlet. The low swirl flow case exhibits a rapid decrease in fuel concentration at the center. This phenomenon occurs as a result of

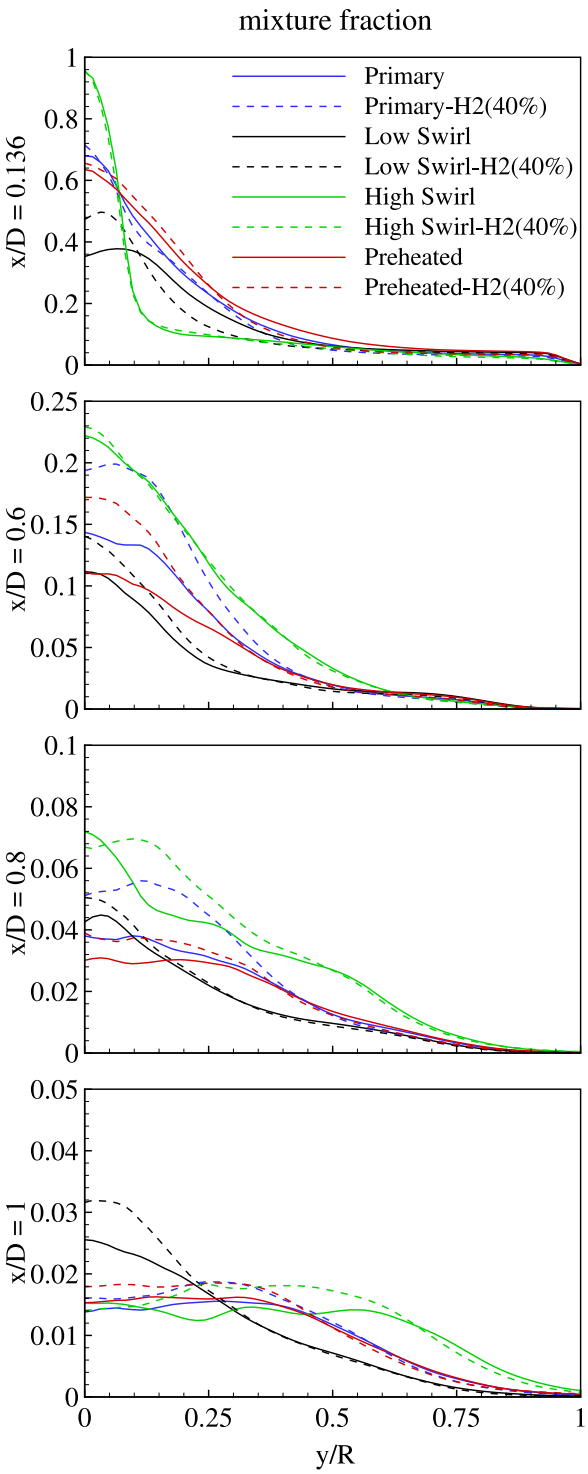

Fig. 10. The mixture fraction profiles at axial distances of x/D = 0.136, 0.6, 0.8, and 1 for four different cases: primary, low swirl, high swirl, and preheated air. The profiles are presented for pure methane (solid line) and a blended fuel with 40% Vol hydrogen and 60% Vol methane (dashed line).

the presence of high TKE in the area, which extends downstream and enhances turbulent mixing.

Fig. 11 demonstrates the mixture fraction profile along the centerline. The addition of hydrogen resulted in a reduction of the slope of fuel concentration decrease in the centerline in all cases except the high swirl case. This decrease in slope is due to the increase in velocity of the fuel inlet jet. In the high swirl case, there is no significant change

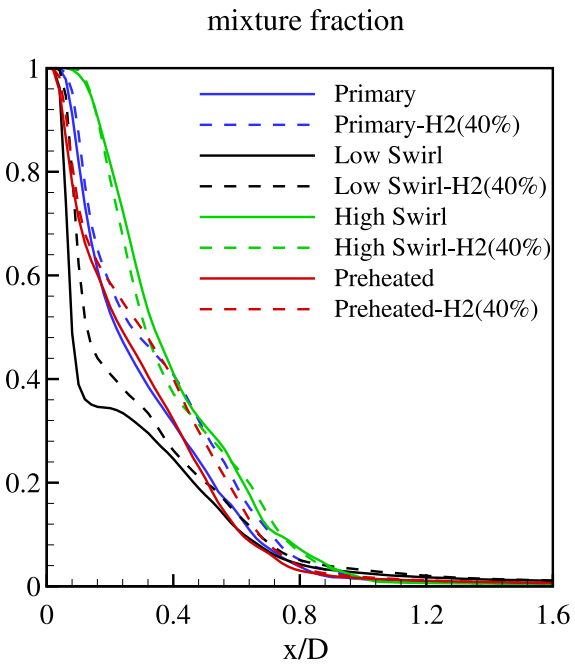

Fig. 11. Mixture fraction profiles along the centerline for four different cases: primary, low swirl, high swirl, and preheated air. The profiles are presented for pure methane (solid line) and blended fuel with 40% Vol hydrogen and 60% Vol methane (dashed line).

in the trend or amount of mixture fraction in the centerline resulting from hydrogen addition to the fuel.

Fig. 12 depicts the instantaneous and averaged two-dimensional views of the mixture fraction for methane fuel. In the primary case, the fuel spreads in a mushroom-like shape, with a slightly larger radius in the radial direction. The low swirl case exhibits the narrowest width in the region with high fuel concentration. The fuel experiences significant stirring at the fuel inlet due to the intensity of TKE and turbulence dissipation rate in this case. The absence of vortex breakdown results in a minor amount of fuel remaining in the center of the flow, which penetrates a longer length to reach stoichiometric levels in the environment. In the high swirl case, a weak mixing near the fuel inlet is observed due to the formation of a bubble around the fuel inlet jet and the low TKE near the bluff body. As the fuel flow passes through the bubble-shaped region, it spreads with greater intensity.

Fig. 13 illustrates the mixture fraction of a hydrogen-methane blend as a fuel. The addition of hydrogen to the fuel reduces the width of the region with high fuel concentration and shifts it downstream in all cases. The least amount of change is observed in the high swirl case.

Fig. 14 illustrates the distribution of methane and hydrogen in the primary, low swirl, high swirl, and preheated cases. The molar percentage of methane and hydrogen at each point was calculated with respect to their percentages at the fuel inlet. The ratio of methane to hydrogen was then calculated, resulting in the fuel distribution ratio (FDR). FDR greater than one indicates a higher concentration of methane than at the fuel inlet, while a ratio below one indicates a higher concentration of hydrogen. In all cases, hydrogen spreads faster than methane due to its lower density and momentum. This effect is most noticeable in the high swirl case, where methane with higher momentum advanced deeper into the axial direction in the bubble region around the fuel jet. However, hydrogen experienced more enhanced stirring in this region. In the preheated case, hydrogen spreads rapidly near the bluff body, leading to a decrease in the width of the concentrated mixture fraction area.

Fig. 15 illustrates the dimensionless averaged stoichiometric volume for each case. In the primary case, the addition of hydrogen decreased

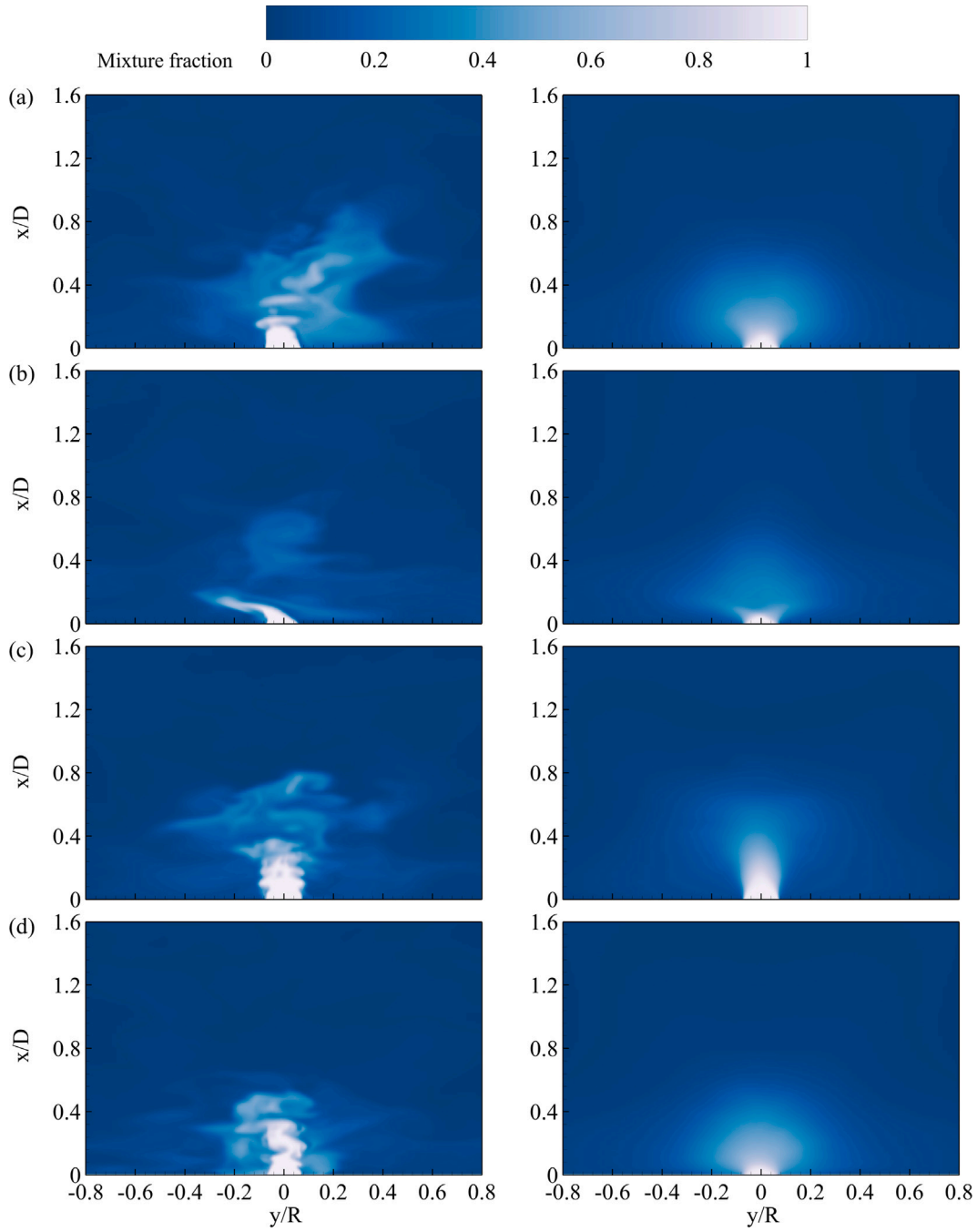

Fig. 12. The mixture fraction contours for four different cases: (a) primary, (b) low swirl, (c) high swirl, and (d) preheated air with methane fuel. The contours are presented for instantaneous (left) and time averaged mixture fraction (right).

the stoichiometric volume by 7%, while increasing the stoichiometric length by 7.5%. At a swirl number of 0.3 compared to the primary case, a reduction of 2% is observed. The stoichiometric length in the high swirl case slightly decreases with the addition of hydrogen. The results shows that in high swirl flow, the stoichiometric length is determined by the size of the bubble formed around the fuel jet. Preheating of inlet air decreases the stoichiometric length compared to the primary case.

The addition of hydrogen to the methane fuel resulted in a decrease in the stoichiometric volume in the primary case, attributed to better hydrogen dispersion and turbulent mixing. The stoichiometric value of the methane-hydrogen blend was 7% lower than pure methane fuel, contributing to a smaller stoichiometric volume. In all flow cases except for the high swirl one, the addition of hydrogen decreases the stoichiometric volume. In the high swirl case, the wider bubble formed around the fuel jet due to the addition of hydrogen results in a stoichiometric surface that reached farther from the fuel jet stream.

4.4. Impact of swirl and preheating on methane-hydrogen mixing

To investigate the effects of swirl and preheating on the mixing of methane-hydrogen fuel with air, simulations are performed for three additional cases, all without swirl: one without preheating, one with preheated fuel, and one with preheated air. These simulations highlight significant differences in both the flow dynamics and the mixing behaviors when compared to the swirling configuration (with 40% volumetric hydrogen).

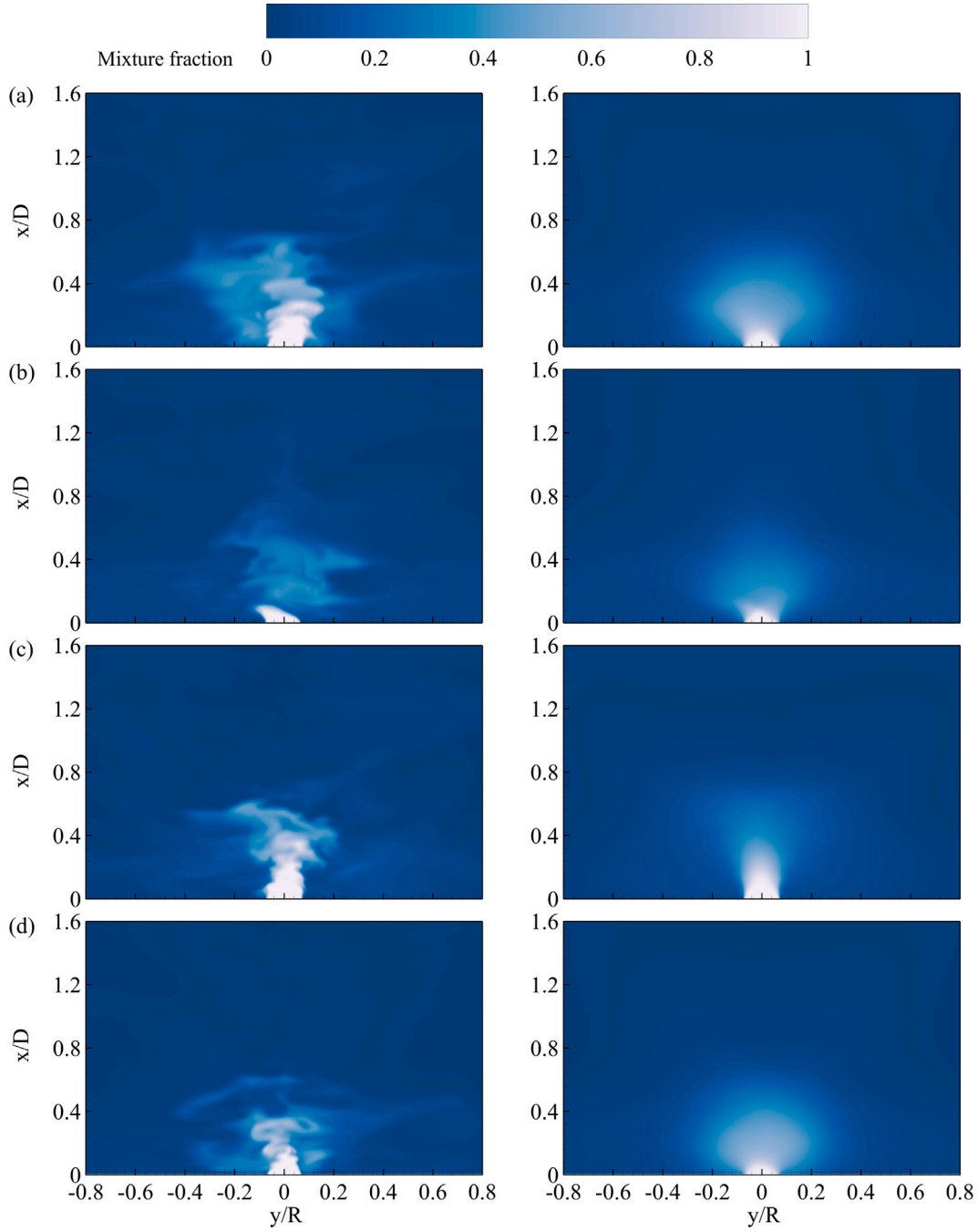

Fig. 13. The mixture fraction contours for four different cases: (a) primary, (b) low swirl, (c) high swirl, and (d) preheated air with a blend of 40% Vol hydrogen and 60% Vol methane fuel. The contours are presented for both instantaneous (left) and time averaged mixture fraction (right).

Fig. 16 illustrates the velocity contours for the three non-swirl cases alongside the primary swirling case. In the absence of swirl, the bluff body induces recirculation zones that merge, forming a continuous recirculation region near the bluff body. In these non-swirl cases, the bluff body's influence is more pronounced and serves as the primary mechanism for generating recirculation zones, which play a critical role in enhancing the air–fuel mixing. With preheated fuel, the fuel stream penetrates deeper into the recirculation zone, causing the zone to narrow. On the other hand, preheating the air results in a thicker recirculation zone, which improves mixing compared to the other cases.

Fig. 17 shows the mixture fraction profiles at different axial positions. The NSNP and NSFP cases demonstrate a higher concentration of the mixture fraction near the centerline at x/D = 0.136, compared to the swirling case. The NSAP case, however, exhibits significant spreading of the mixture fraction, starting near the bluff body. This enhanced mixing behavior in the NSAP case can be attributed to a higher momentum flux ratio between the fuel and the preheated air.

Fig. 18 presents the mixture fraction profiles along the centerline. Preheating the air leads to a more rapid reduction in fuel concentration along the centerline, indicating improved mixing efficiency. The degree of fuel spreading in the non-swirl cases is directly related to the size of the recirculation zone, which in turn is influenced by the preheating conditions and the absence of swirl.

The absence of swirl flow leads to faster and more efficient mixing downstream of the bluff body, but several critical challenges make swirl flow regimes essential in practical combustion systems. One significant

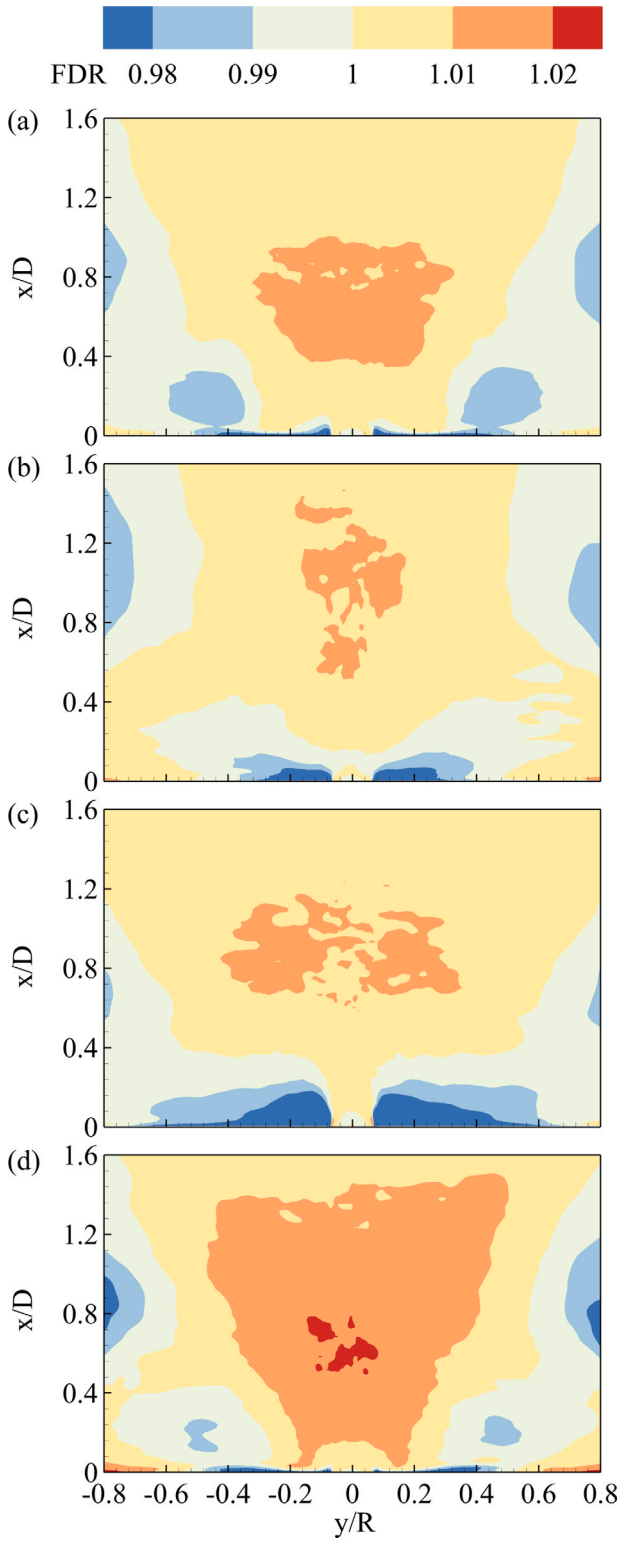

Fig. 14. The contours of FDR for four different cases: (a) primary, (b) low swirl, (c) high swirl, and (d) preheated air.

issue is that increased fuel jet velocity can cause the jet to penetrate and bypass the recirculation zone. This behavior is evident in the preheated fuel case, where the higher velocity enables deeper penetration compared to the non-preheated case. Without the stabilizing influence of swirl, there is no mechanism to counter this, potentially reducing the blow-off limit. Additionally, in the absence of swirl, the flame tends to stabilize closer to the burner surface, increasing the risk of thermal damage to the burner. Another concern is that the reduced flame surface area without swirl decreases heat transfer efficiency.

Furthermore, the shorter recirculation zone without swirl allows reaction products to exit more quickly. In contrast, swirl flow induces vortex breakdown, generating a more downstream recirculation zone, which enhances combustion stability and helps control emissions. Overall, swirl flow structures offer better control over combustion stability, heat transfer, and emissions management, making them indispensable in practical applications.

4.5. *Turbulence and statistics of mixing*

The variance spectral density (VSD) for different cases at the centerline and x/D = 0.6 is presented in Fig. 19. The VSD profiles of methane and hydrogen mass concentration show similar variations, indicating that eddies with specific frequencies play comparable roles for both. Consequently, the turbulent mass transfer in the resolved range in LES is a function of the flow field, rather than fluid properties. This confirms the validity of the assumption of a constant turbulence diffusion coefficient for all species. However, differences in fluid characteristics are observed at high frequencies and in regions modeled by SGS. Neglecting such differences during the modeling of high frequencies is a source of error in turbulent flow calculations using LES. Since the area under the graphs after cut-off frequencies to the total area under the graph is minimal, the modeling error resulting from SGS modeling is small in proportion. Moreover, Fig. 19 reveals that the eddies at the beginning of the inertial range for momentum perform as integral eddies for turbulent mass transfer. The contribution of each frequency range of eddies in turbulence mass and momentum transfer is indicates by the area under each region.

Fig. 20 displays the Probability Density Function (PDF) of the mixture fraction for two cross-sections at x/D = 0.136 and 0.6 and four radial positions. A non-marching PDF exhibits a peak value that is quasi-independent of the radial position and distinct from the mean value, while a marching PDF exhibits a peak value that equals the mean value. Large-scale mixing results in a non-marching PDF, whereas small-scale mixing leads to marching behavior [8]. The primary case displays marching behavior at x/D = 0.136 and y/R = 0.2 and 0.6, where the first spot is situated in a boundary of a small recirculation zone. Conversely, the behavior of the PDF is non-marching at x/D = 0.6 and the continuous point section, indicating the dominance of large turbulence structures in these regions. In the low swirl case, both the x/D = 0.136 and 0.6 and y/R = 0.0, 0.2, and 0.4 exhibit non-marching PDF behavior. In contrast, the high swirl case, unlike the primary and low swirl, displays marching behavior at x/D = 0.136 in all positions. The preheated air case exhibits almost the same variation as the primary case, except for the non-marching behavior at x/D = 0.136 and y/R = 0.2. Absence of the recirculation region is responsible for the non-marching behavior at mentioned sections.

Fig. 21 illustrates the effect of adding hydrogen on the PDF. At y/R=0, the addition of hydrogen suppresses the variation of PDF, indicating a higher probability of the occurrence of a certain mixture fraction ranges that are less likely in the case of pure methane. However, this behavior is reversed to some extent for points out of the centerline (y/R> 0) where blending fuel with hydrogen leads to a more concentrated PDF around the peak of its profile.

Fig. 22 illustrates the scalar dissipation rate (SDR) contours for present studied flow cases. The SDR is defined as follow [40]:

$$\mathrm{SDR} = 2\left(D_m + D_t\right)\left(\nabla\overline{\zeta}\right)^2. \tag{7}$$

In the primary flow case, a small area with a low SDR is visible at the fuel inlet. High velocity flow at the fuel inlet prevents sufficient air intake, resulting in a less steep gradient in the mixture fraction. The

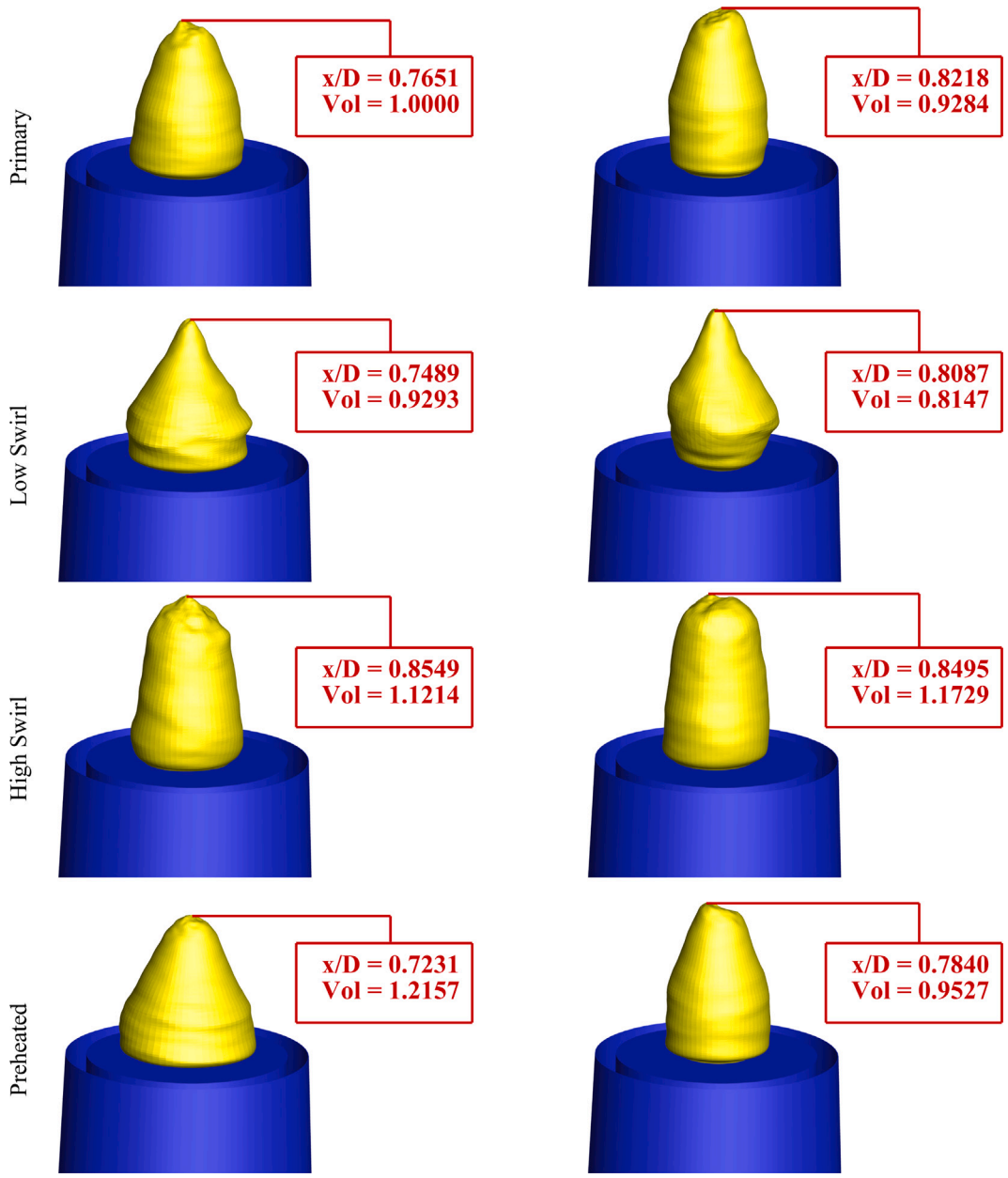

Fig. 15. The stoichiometric volume for four different cases: primary, low swirl, high swirl, and preheated air. The stoichiometric volume are presented for pure methane (left) and blended fuel with 40% Vol hydrogen and 60% Vol methane (right).

dissipation rate of the mixture fraction increases in the region with high shear stress between the high-velocity area near the fuel jet and the low-energy area close to the bluff body surface. In the low swirl flow case, the dispersion rate of the mixture fraction increases by relatively high TKE calculated at the inlet of fuel jet. In the high swirl flow case, a region with a significantly high SDR is observable near the boundary of the bubble around the fuel jet. This region originates from the intense shear stress between the recirculation region outside and the high velocity region inside the bubble. These high SDR areas result from the strong stretching of vortices, which increases significantly the gradient of the mixture fraction. Preheating air and increasing the momentum flux ratio between the fuel and air flow create more regions with higher SDR compared to the primary case. The addition of hydrogen to the fuel considerably enhances the mixing, as indicated by the increase in high SDR regions.

Fig. 23 illustrates the intensity of segregation (IS) for different cases expressed by [41]:

$$\mathrm{IS} = \frac{\overline{\zeta'^2}}{\bar{\zeta}(1-\bar{\zeta})} \tag{8}$$

In the primary flow case, hydrogen addition leads to a decrease in the areas with high IS, and enhances the turbulent mixing. The low swirl flow case exhibits the lowest amount of IS compared to all other cases, which is increased by the addition of hydrogen in the high IS region at the fuel jet entrance. This increase can be attributed as a rapid rise in inlet jet velocity resulting from the absence of a control mechanism such as vortex breakdown. For high swirl flow case, the inlet area of the fuel jet remains unchanged as the hydrogen is added, but the mixing quality is improved at downstream. Furthermore, in the preheated case, the concentration of high IS regions is reduced by adding hydrogen.

Fig. 24 demonstrates the uncertainty resulting from potential errors in SGS modeling. In this study, OpenFOAM utilizes implicit filtering

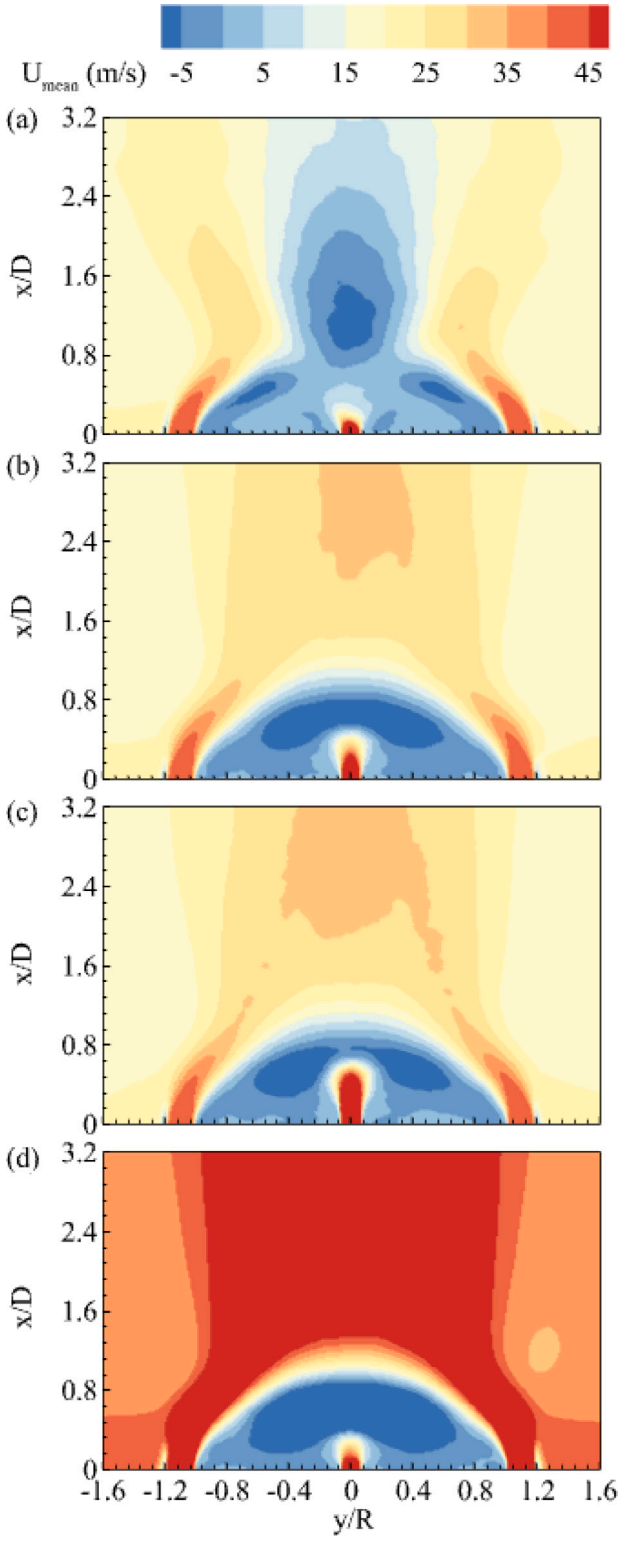

Fig. 16. Axial velocity contours for four different cases: (a) primary, (b) NSNP, (c) NSFP, and (d) NSAP.

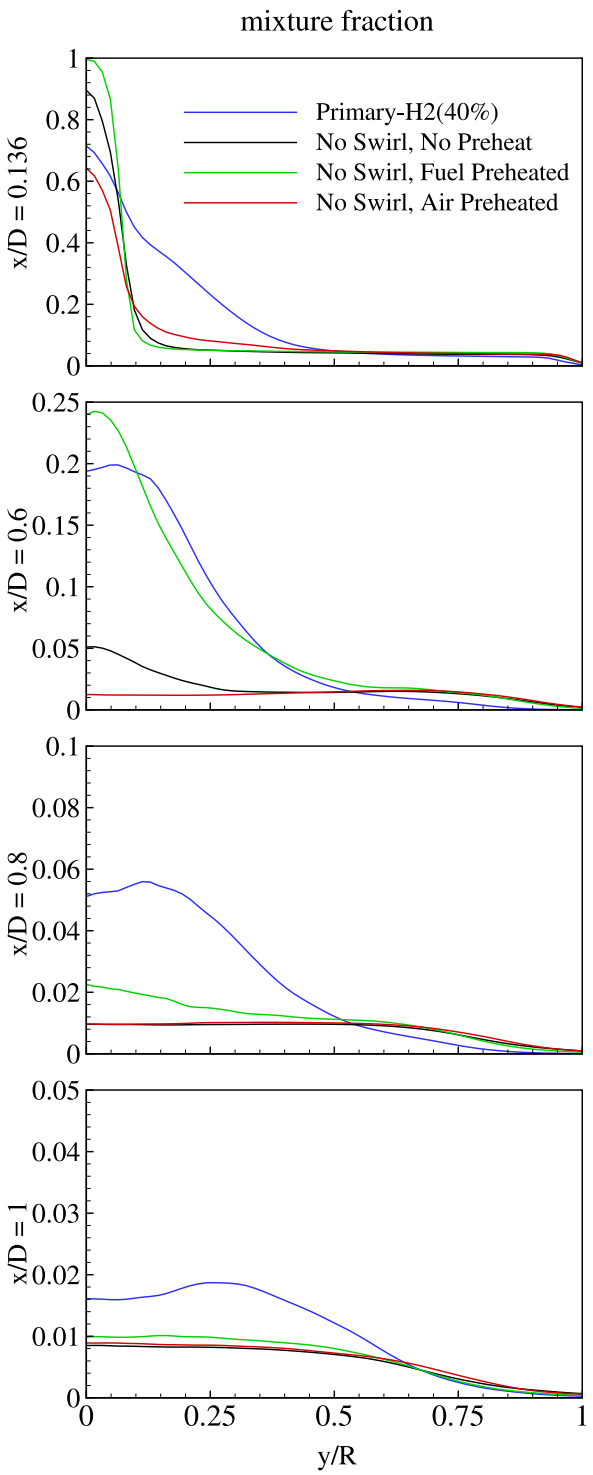

Fig. 17. The mixture fraction profiles at axial distances of x/D = 0.136, 0.6, 0.8, and 1 for four different cases: primary, NSNP, NSFP, and NSAP.

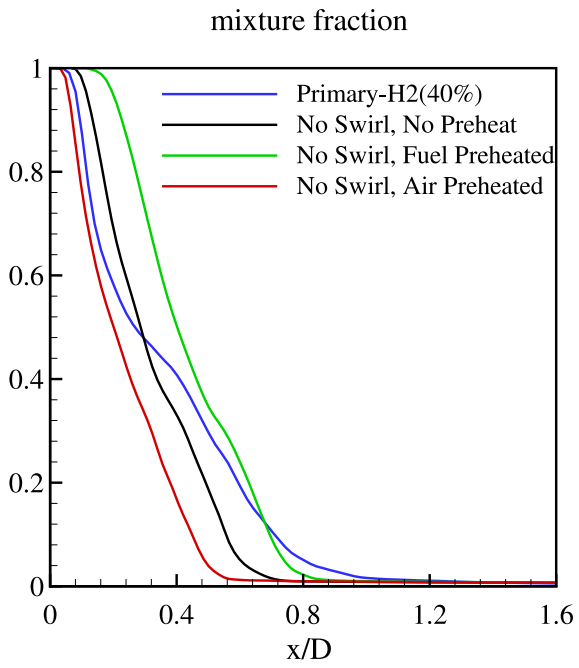

Fig. 18. Mixture fraction profiles along the centerline for four different cases: primary, NSNP, NSFP, and NSAP.

with equivalent filter and grid sizes. Assuming equal filter and grid size, the numerical error is of the same order of magnitude as the SGS modeling error [42]. Moreover, the SGS modeling error can be estimated by comparing resolved and total TKE suggested by Lozano-Durán and Bae [43] for the outer region of wall turbulence. The figure provides an estimate of the error range for flow field parameters, such as turbulence intensity and velocity field. The molecular and turbulence Schmidt numbers of the fuel composition are approximately one and lower, respectively. Based on the Schmidt number, the size of the smallest turbulence scale of mass concentration is greater than or equal to the smallest turbulence scale in velocity [44,45]. Hence, the uncertainty depicted in Fig. 24 is also applicable to mixing. Notably, the maximum value of SGS modeling uncertainty in stoichiometric regions is less than 2.5% in all cases, indicating the reliability of the results.

5. Conclusion

This study investigated the mixing characteristics of air, methane, and hydrogen by varying the swirl number, air preheating, and hydrogen addition to methane. The results revealed important insights into the effects of these parameters on the flow field and mixing behavior in coflow-swirl jets, with a particular focus on hydrogen addition to methane as a fuel. These findings contribute to a deeper understanding of hydrogen-blended fuel dynamics, which is crucial for the advancement of sustainable combustion technologies.

The flow structures, including recirculation bubbles, zones, neck regions, and collar-like flows, were found to be primarily influenced by the fuel and air mass flow rates and swirl number. While hydrogen addition and air preheating had a moderate effect, the dominant factor was the swirl number, which shaped the overall flow behavior. Increasing the swirl number expanded the recirculation zones and created bubble-shaped areas around the fuel jet stream, leading to weaker mixing. This demonstrates the important role of swirl in controlling the flow field and highlights the need for careful management of swirl levels to optimize mixing efficiency.

Hydrogen addition led to a significant increase in the velocity of the fuel jet, especially in low swirl cases. This was due to the absence of vortex breakdown, a phenomenon that typically acts as a control mechanism for fuel jet velocity. Hydrogen, having a lower density than methane, was more easily influenced by the flow field and spread more rapidly, enhancing fuel dispersion. Additionally, the hydrogen-enriched fuel increased the turbulent kinetic energy at the fuel jet inlet, a result of the higher fuel jet velocity and the energy imbalance in the surrounding fluid layers, which was caused by the differing momentum of the hydrogen and methane.

Furthermore, hydrogen addition altered the mixture fraction along the centerline. In most cases, the slope of the mixture fraction decreased with hydrogen, except in high swirl cases where bubble-shaped structures regulated the mixing. This shift in the mixing characteristics expect to affect the stoichiometry area and flame stability. The scalar dissipation rate increased with hydrogen addition, which led to reduced segregation intensity and generally improved mixing quality. However, in cases without vortex breakdown, mixing was less efficient in the initial stages of the fuel jet entering the domain.

The absence of swirl flow resulted in faster and more efficient mixing near the bluff body surface. However, this can introduce several challenges, including blow-off limitations, increased risk of thermal damage to the burner, inefficient heat transfer, flame instability, and higher pollutant emissions. Consequently, swirl flow structures are essential for enhancing combustion stability, improving heat transfer efficiency, and managing emissions effectively in practical combustion applications.

A key finding of this study is that preheating the air proves to be an effective method for enhancing mixing in both swirl and non-swirl regimes. Depending on the design goals, preheating can influence the flame's proximity to the burner surface. Air preheating tends to bring the flame surface closer to the burner, while preheating the fuel pushes it further away, both of which contribute to improved mixing. In non-swirl burners, air preheating is particularly beneficial, as it enhances mixing and helps prevent the fuel stream from bypassing the recirculation zone. This makes air preheating a practical approach for optimizing combustion efficiency and stability.

It is expected that in reacting flows with the same boundary conditions and geometry as the non-reactive cases studied here, the flow structures will remain similar, with their positions varying due to higher flow velocities and increased heat transfer in reactive conditions.

Overall, the insights gained from this study offer valuable guidance for optimizing hydrogen-methane fuel blends. The careful consideration of swirl, hydrogen addition, and preheating is crucial in shaping the flow field and enhancing mixing, thereby paving the way for the development of cleaner and more efficient combustion systems.

CRediT authorship contribution statement

Amin Bekhradinasab: Writing – original draft, Visualization, Software, Methodology. **Shidvash Vakilipour:** Writing – review & editing, Supervision, Methodology, Investigation. **Jafar Al-Zaili:** Writing – review & editing, Supervision, Resources, Conceptualization.

Declaration of competing interest

The authors declare that they have no known competing financial interests or personal relationships that could have appeared to influence the work reported in this paper.

Data availability

Data will be made available on request.

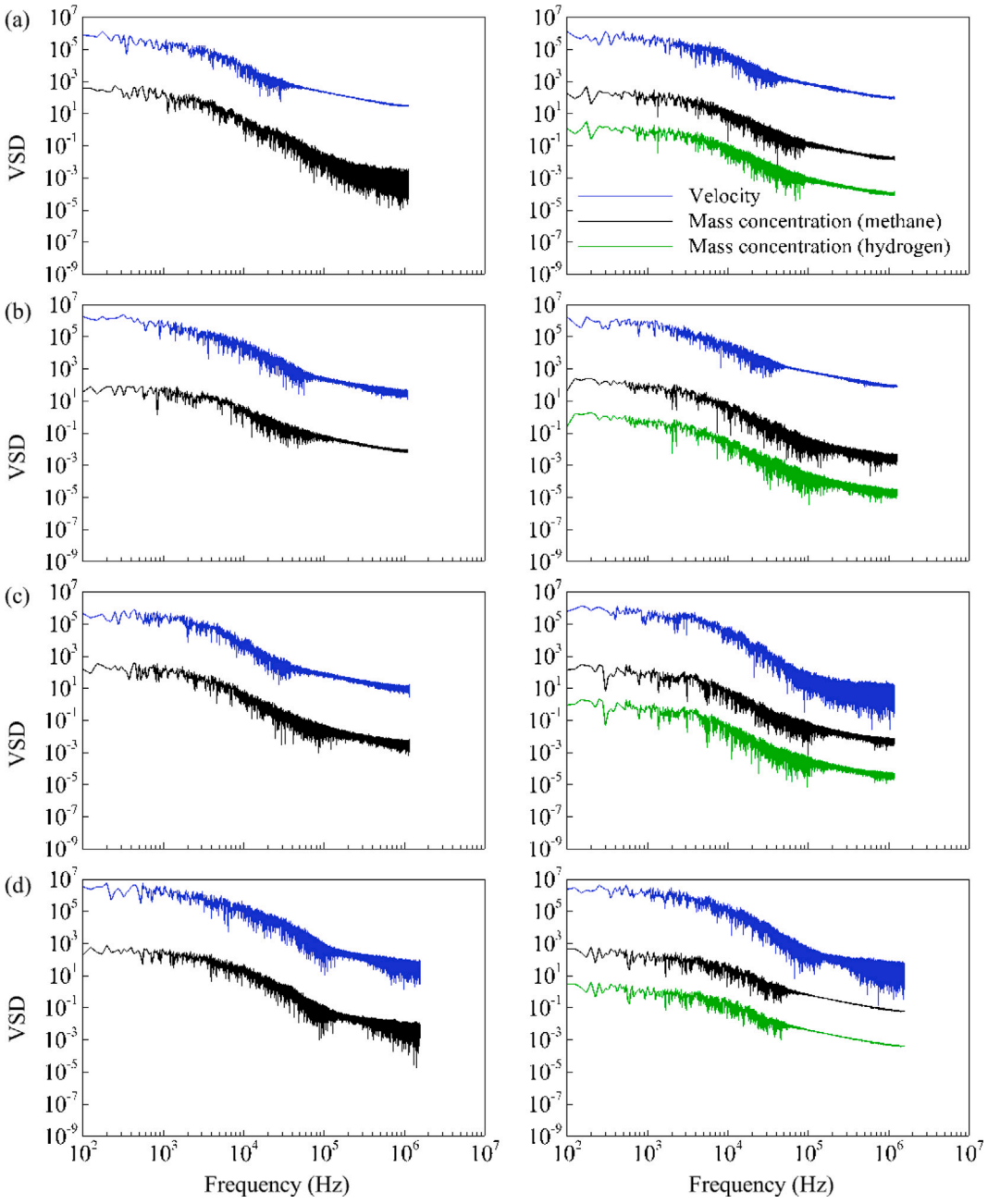

Fig. 19. The VSD profiles along the centerline at x/D = 0.6 for four different cases: (a) primary, (b) low swirl, (c) high swirl, and (d) preheated air. The profiles are presented for pure methane (left) and blended fuel with 40% Vol hydrogen and 60% Vol methane (right).

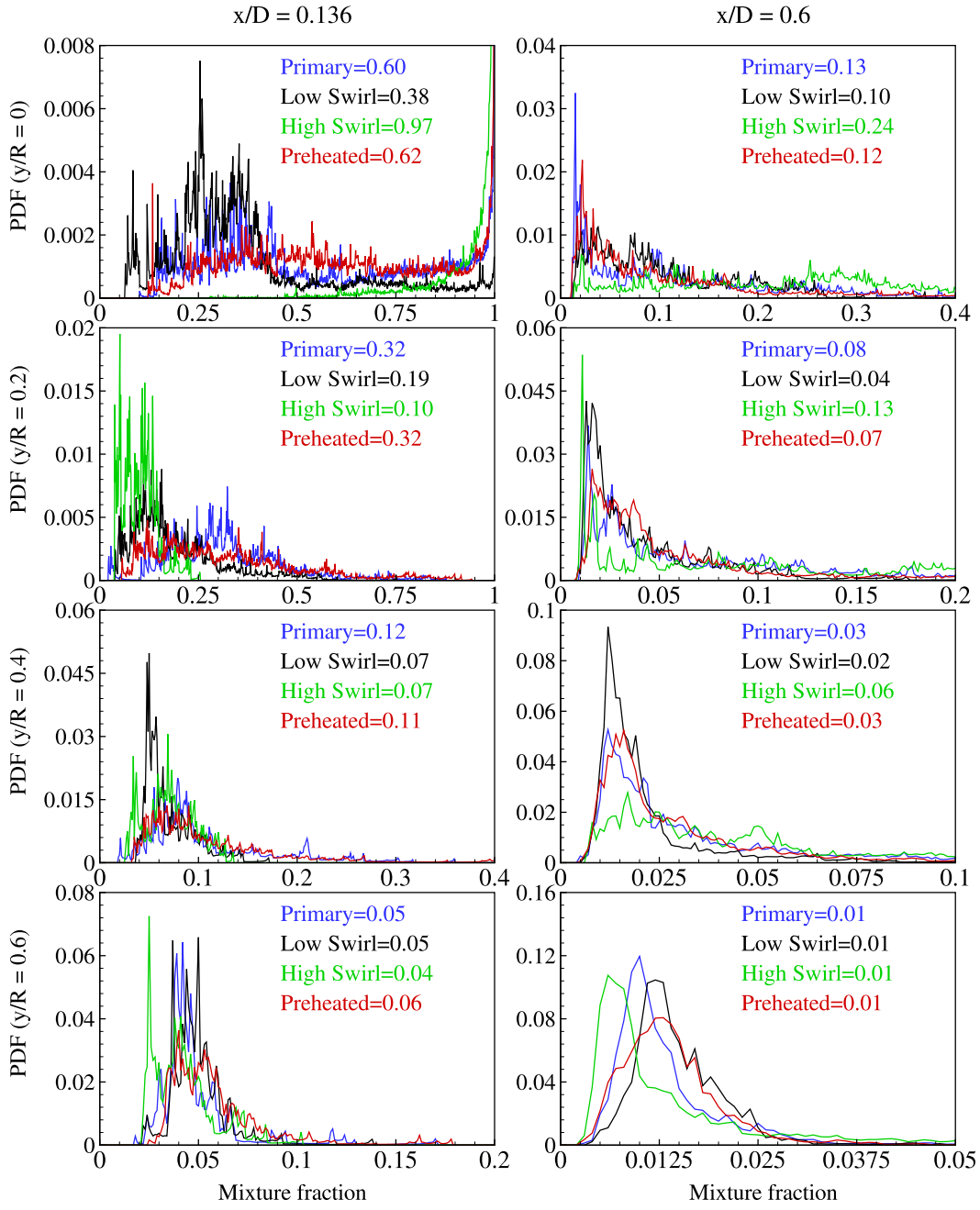

Fig. 20. The PDF of the mixture fraction across the radial direction at x/D = 0.136 and x/D = 0.6 for pure methane. The average mixture fraction for each point and case is indicated.

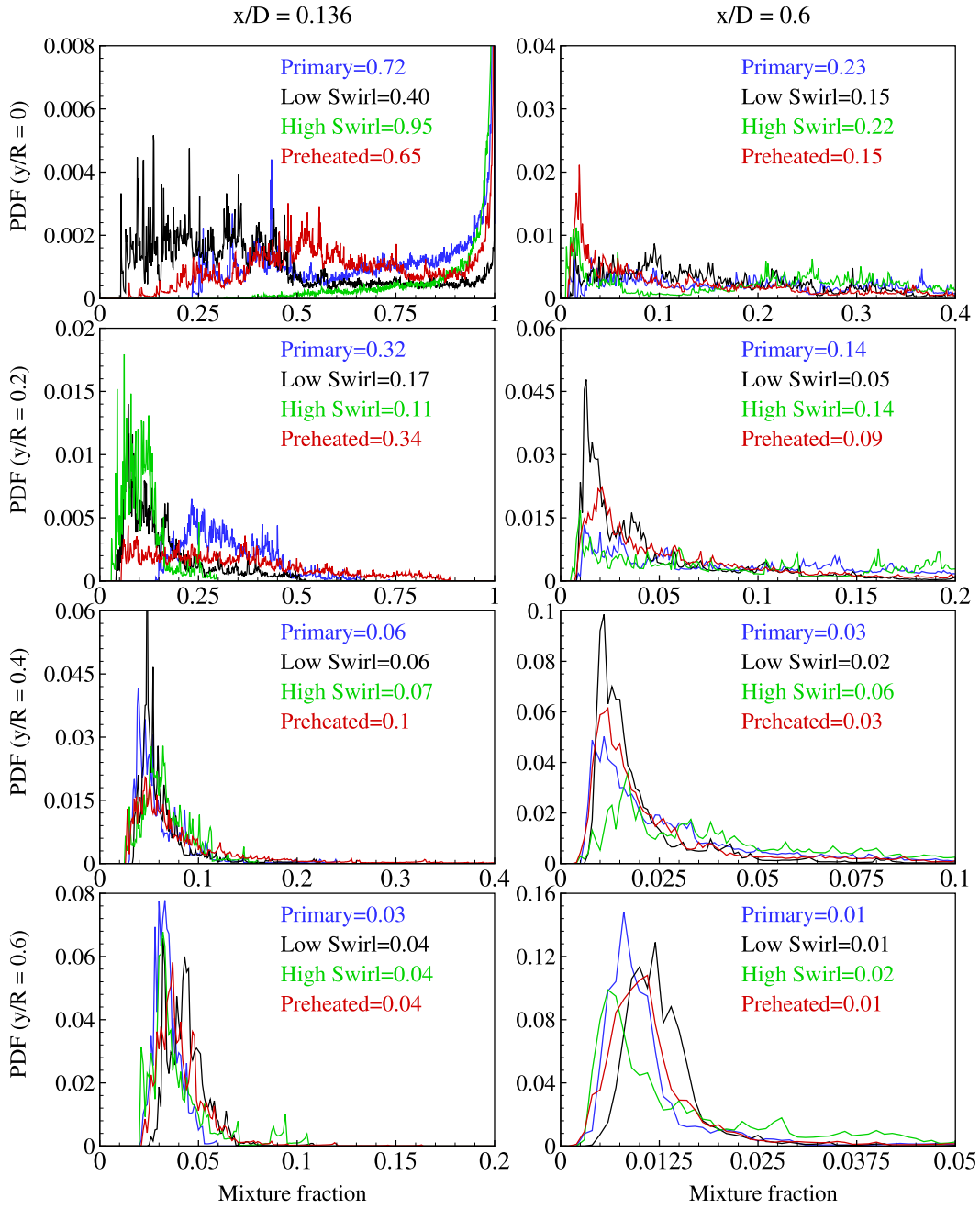

Fig. 21. Variation of PDF of the mixture fraction at points with x/D = 0.136 and x/D = 0.6 and selected radial distance for the blended fuel with 40% Vol hydrogen and 60% Vol methane. The average mixture fraction is indicated for each point and case.

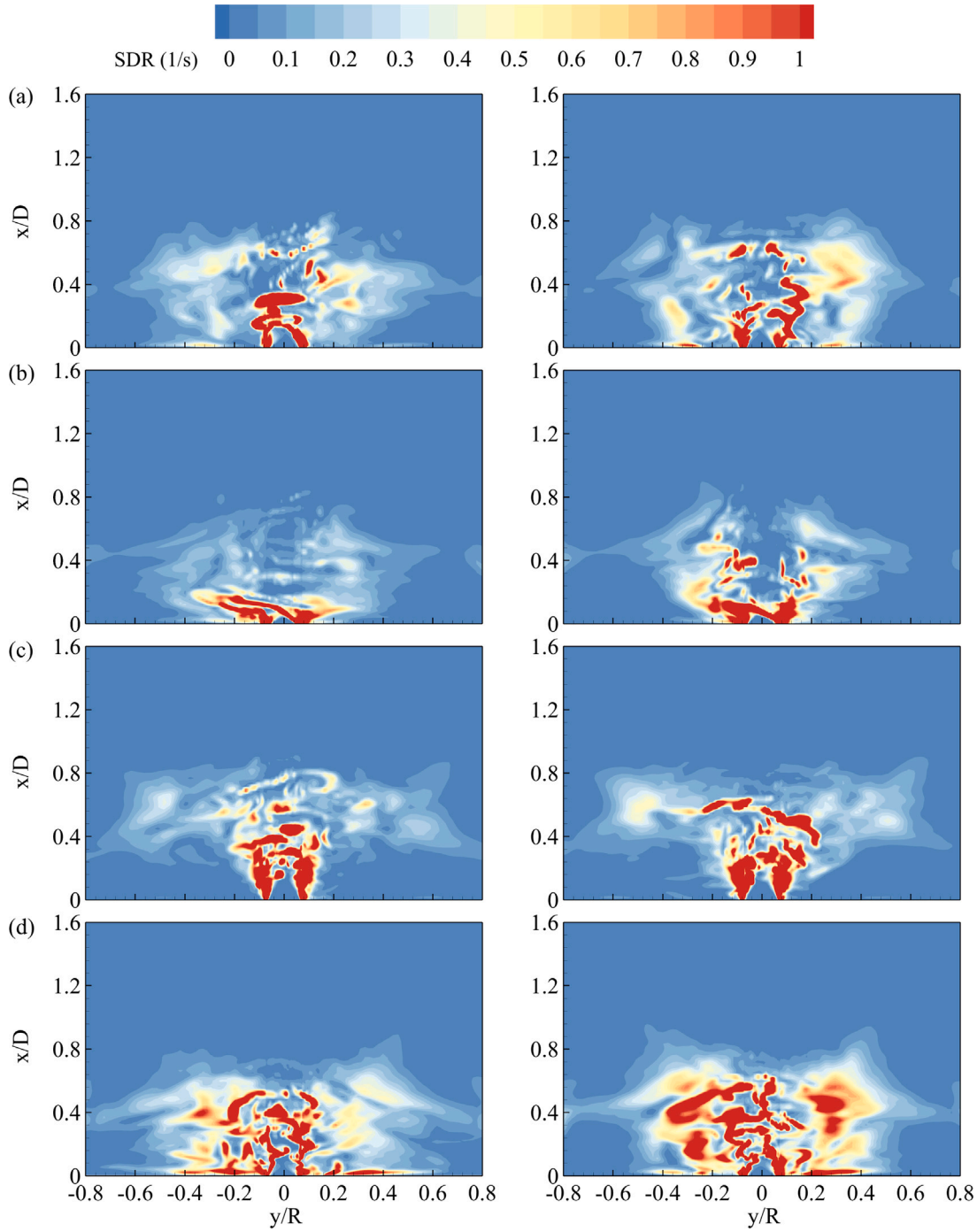

Fig. 22. SDR contours for four studied cases: (a) primary, (b) low swirl, (c) high swirl, and (d) preheated air. The contours are presented for pure methane fuel (left) and blended fuel with 40% Vol hydrogen and 60% Vol methane (right).

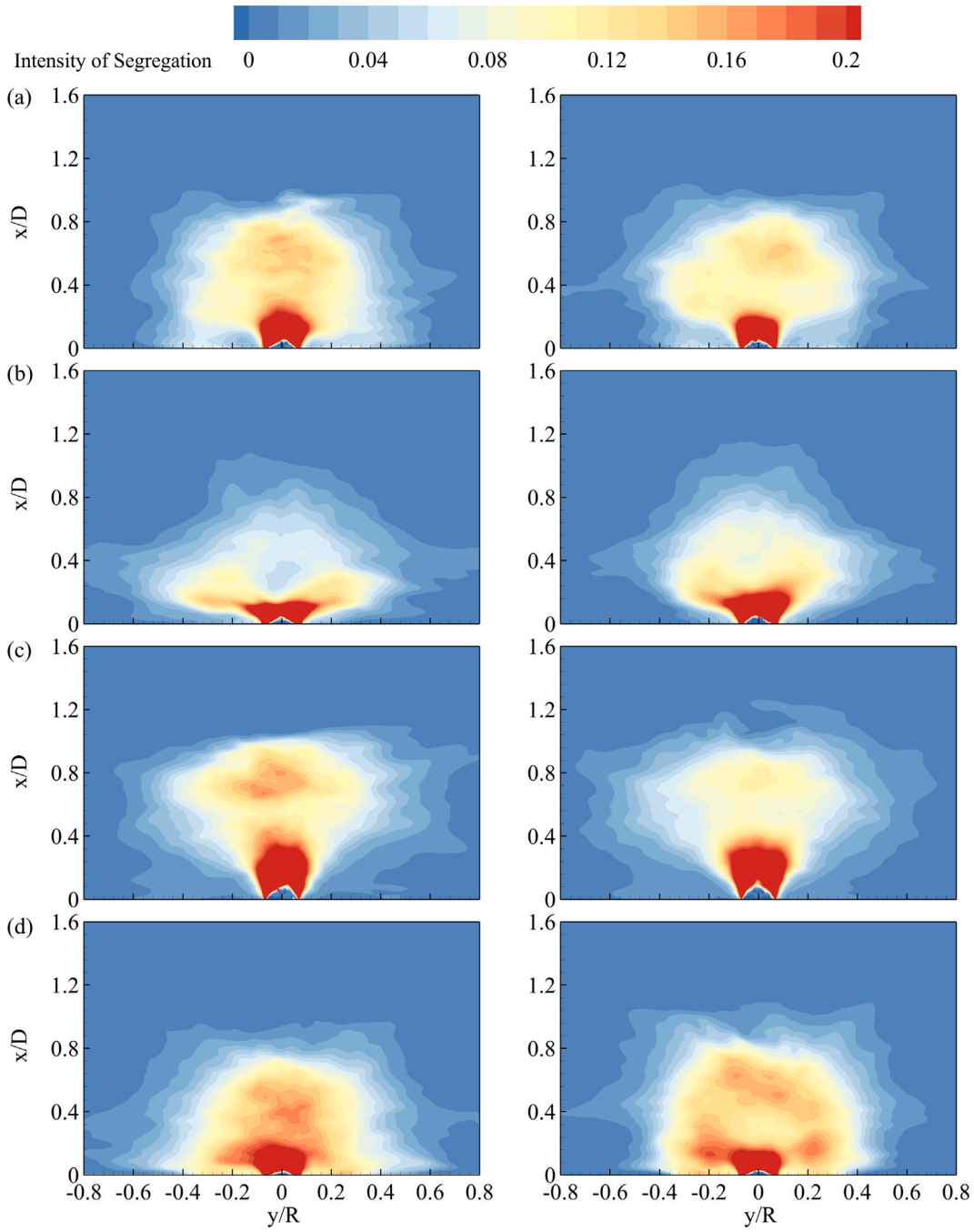

Fig. 23. The IS contours for four studied cases: (a) primary, (b) low swirl, (c) high swirl, and (d) preheated air. The contours are presented for pure methane fuel (left) and blended fuel with 40% Vol hydrogen and 60% Vol methane (right).

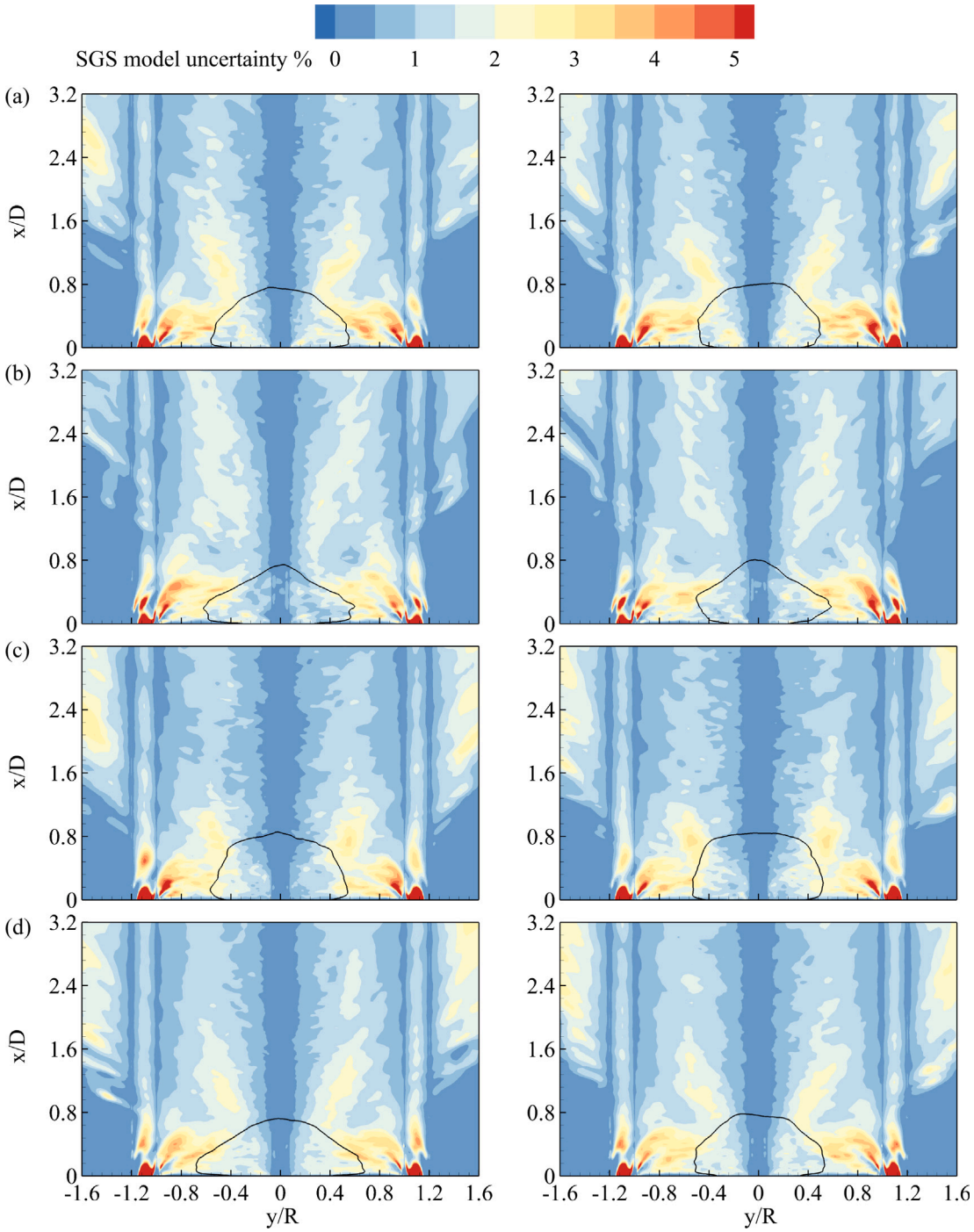

Fig. 24. The SGS modeling uncertainty contours for four different cases: (a) primary, (b) low swirl, (c) high swirl, and (d) preheated air. The contours are presented for both methane fuel (left) and blended fuel with 40% Vol hydrogen and 60% Vol methane (right). Solid lines indicate location of stoichiometric mixture fraction.

References

[1] K.R. Sreenivasan, Turbulent mixing: A perspective, Proc. Natl. Acad. Sci. 116 (2019) 18175–18183.

[2] P.E. Dimotakis, Turbulent mixing, Annu. Rev. Fluid Mech. 37 (2005) 329–356.

[3] J. Kim, P. Moin, Transport of passive scalars in a turbulent channel flow, in: Turbulent Shear Flows 6, Springer, 1989, pp. 85–96.

[4] M. Holzer, E.D. Siggia, Turbulent mixing of a passive scalar, Phys. Fluids 6 (1994) 1820–1837.

[5] C. Tong, Z. Warhaft, Passive scalar dispersion and mixing in a turbulent jet, J. Fluid Mech. 292 (1995) 1–38.

[6] R. Bergant, I. Tiselj, Near-wall passive scalar transport at high Prandtl numbers, Phys. Fluids 19 (2007) 065105.

[7] A. Bekhradinasab, J. Al-Zaili, S. Vakilipour, Large eddy simulation of separated flow to investigate heat transfer characteristics in an asymmetric diffuser subjected to constant wall heat flux, Int. Commun. Heat Mass Transfer 128 (2021) 105634.

[8] G. Balarac, O. Métais, M. Lesieur, Mixing enhancement in coaxial jets through inflow forcing: A numerical study, Phys. Fluids 19 (2007) 075102.

[9] S. Alexander Schumaker, J.F. Driscoll, Mixing properties of coaxial jets with large velocity ratios and large inverse density ratios, Phys. Fluids 24 (2012) 055101.

[10] A. Masri, S. Pope, B. Dally, Probability density function computations of a strongly swirling nonpremixed flame stabilized on a new burner, Proc. Combust. Inst. 28 (2000) 123–131.

[11] P.A. Kalt, Y.M. Al-Abdell, A.R. Masri, R.S. Barlow, Swirling turbulent non-premixed flames of methane: flow field and compositional structure, Proc. Combust. Inst. 29 (2002) 1913–1919.

[12] Y.M. Al-Abdeli, A.R. Masri, Stability characteristics and flowfields of turbulent non-premixed swirling flames, Combust. Theory Model. 7 (2003) 731.
[13] W. Malalasekera, K. Ranga-Dinesh, S.S. Ibrahim, A.R. Masri, LES of recirculation and vortex breakdown in swirling flames, Combust. Sci. Technol. 180 (2008) 809–832.
[14] S. Vakilipour, Y. Tohidi, J. Al-Zaili, R. Riazi, A numerical investigation of CO2 dilution on the thermochemical characteristics of a swirl stabilized diffusion flame, Appl. Math. Mech. 41 (2020) 327–348.
[15] C.O. Paschereit, E. Gutmark, W. Weisenstein, Coherent structures in swirling flows and their role in acoustic combustion control, Phys. Fluids 11 (1999) 2667–2678.
[16] M. Escudier, Vortex breakdown: observations and explanations, Prog. Aerosp. Sci. 25 (1988) 189–229.
[17] D. Froud, T. O'doherty, N. Syred, Phase averaging of the precessing vortex core in a swirl burner under piloted and premixed combustion conditions, Combust. Flame 100 (1995) 407–412.
[18] C. Meraner, T. Li, M. Ditaranto, T. Lø vås, Cold flow characteristics of a novel bluff body hydrogen burner, Int. J. Hydrog. Energy 43 (2018) 7155–7168.
[19] Y.M. Al-Abdeli, A.R. Masri, Recirculation and flowfield regimes of unconfined non-reacting swirling flows, Experiment. Thermal Fluid Sci. 27 (2003) 655–665.
[20] Y.M. Al-Abdeli, A.R. Masri, Precession and recirculation in turbulent swirling isothermal jets, Combust. Sci. Technol. 176 (2004) 645–665.
[21] W. Malalasekera, K. Ranga Dinesh, S. Ibrahim, M. Kirkpatrick, Large eddy simulation of isothermal turbulent swirling jets, Combust. Sci. Technol. 179 (2007) 1481–1525.
[22] K.R. Dinesh, M. Kirkpatrick, Study of jet precession, recirculation and vortex breakdown in turbulent swirling jets using LES, Comput. & Fluids 38 (2009) 1232–1242.
[23] K.R. Dinesh, K. Jenkins, A. Savill, M. Kirkpatrick, Swirl effects on external intermittency in turbulent jets, Int. J. Heat Fluid Flow 33 (2012) 193–206.
[24] Y. Yang, S.r.K. Kær, Large-eddy simulations of the non-reactive flow in the Sydney swirl burner, Int. J. Heat Fluid Flow 36 (2012) 47–57.
[25] M. Gu, Q. He, F. Tang, Experimental and machine learning studies of thermal impinging flow under ceiling induced by hydrogen-blended methane jet fire: Temperature distribution and flame extension characteristics, Int. J. Heat Mass Transfer 215 (2023) 124502.
[26] Z. Li, N.H. Abu-Hamdeh, A. Musa, Y. Zhang, Influence of downstream ramp on mass diffusion of various coaxial hydrogen and air injectors at supersonic combustion chamber, Int. J. Heat Mass Transfer 199 (2022) 123460.
[27] Y. Afarin, S. Tabejamaat, Effect of hydrogen on H2/CH4 flame structure of mild combustion using the LES method, Int. J. Hydrog. Energy 38 (2013) 3447–3458.
[28] S. Hashemi, A. Fattahi, G. Sheikhzadeh, M. Mehrabian, Investigation of the effect of air turbulence intensity on NOx emission in non-premixed hydrogen and hydrogen-hydrocarbon composite fuel combustion, Int. J. Hydrogen Energy 36 (2011) 10159–10168.
[29] B. Kashir, S. Tabejamaat, N. Jalalatian, On large eddy simulation of blended CH4–H2 swirling inverse diffusion flames: The impact of hydrogen concentration on thermal and emission characteristics, Int. J. Hydrog. Energy 40 (2015) 15732–15748.
[30] A.R. Tajik, P. Kuntikana, S.V. Prabhu, V. Hindasageri, Effect of preheated mixture on heat transfer characteristics of impinging methane–air premixed flame jet, Int. J. Heat Mass Transfer 86 (2015) 550–562.
[31] A. De Santis, A.G. Clements, A. Pranzitelli, D.B. Ingham, M. Pourkashanian, Assessment of the impact of subgrid-scale stress models and mesh resolution on the LES of a partially-premixed swirling flame, Fuel 281 (2020) 118620.
[32] A. Favre, Turbulence: Space-time statistical properties and behavior in supersonic flows, Phys. Fluids 26 (1983) 2851–2863.
[33] X. Xu, J.S. Lee, R.H. Pletcher, A compressible finite volume formulation for large eddy simulation of turbulent pipe flows at low Mach number in Cartesian coordinates, J. Comput. Phys. 203 (2005) 22–48.
[34] S. Zhong, F. Zhang, M. Jangi, X.-S. Bai, M. Yao, Z. Peng, Structure and propagation of n-heptane/air premixed flame in low temperature ignition regime, Appl. Energy 275 (2020) 115320.
[35] C. Wilke, A viscosity equation for gas mixtures, J. Chem. Phys. 18 (1950) 517–519.
[36] S. Zhong, F. Zhang, Z. Peng, F. Bai, Q. Du, Roles of CO2 and H2O in premixed turbulent oxy-fuel combustion, Fuel 234 (2018) 1044–1054.
[37] J. Jeon, D. Shin, W. Choi, S.J. Kim, Identification of the extinction mechanism of lean limit hydrogen flames based on Lewis number effect, Int. J. Heat Mass Transfer 174 (2021) 121288.
[38] M. Dutka, M. Ditaranto, T. Lø vås, NOx emissions and turbulent flow field in a partially premixed bluff body burner with CH4 and H2 fuels, Int. J. Hydrog. Energy 41 (2016) 12397–12410.
[39] R. Bilger, S. Stårner, R. Kee, On reduced mechanisms for methane air combustion in nonpremixed flames, Combust. Flame 80 (1990) 135–149.
[40] C. Jiménez, F. Ducros, B. Cuenot, B. Bédat, Subgrid scale variance and dissipation of a scalar field in large eddy simulations, Phys. Fluids 13 (2001) 1748–1754.
[41] M. Muradoglu, H.A. Stone, Mixing in a drop moving through a serpentine channel: A computational study, Phys. Fluids 17 (2005) 073305.
[42] I. Celik, Z. Cehreli, I. Yavuz, Index of resolution quality for large eddy simulations, 2005.
[43] A. Lozano-Durán, H.J. Bae, Error scaling of large-eddy simulation in the outer region of wall-bounded turbulence, J. Comput. Phys. 392 (2019) 532–555.
[44] H. Tennekes, J.L. Lumley, J.L. Lumley, et al., A First Course in Turbulence, MIT Press, 1972.
[45] H. Kawamura, K. Ohsaka, H. Abe, K. Yamamoto, DNS of turbulent heat transfer in channel flow with low to medium-high Prandtl number fluid, Int. J. Heat Fluid Flow 19 (1998) 482–491.